Mesh refinement procedures for the phase field approach to brittle fracture

Mesh refinement procedures for the phase field approach to brittle fracture

F. Freddi[a,*], L. Mingazzi[a]

[a]*Department of Engineering and Architecture, University of Parma, Parco Area delle Scienze 181/A, 43124 Parma, Italy*

Abstract

Two refinement procedures for phase field approach are proposed and their numerical performances are investigated in the solution of fracture problems. Starting from a coarse discretization of the domain, an energetic criterion is used to determine the active zones where damage initiates, evolves and mesh refinement is mandatory to accurately approximate crack topology. Moreover, the extension of the refined regions is strictly correlated with the size of the process zone defined by the optimal profile. Global and global/local refinement strategies are investigated. In particular, the global/local technique solves the displacement and phase field problems on a local mesh dynamically updated and adaptively refined during the computation. Once the solutions of the local problems are obtained, the phase field is interpolated back onto the original mesh, adequately refined where a damage threshold is exceeded. The performances of the refinement techniques are analysed and compared in representative examples with stable and brutal crack propagation.

Keywords: variational fracture mechanics, phase field, adaptive refinement, global/local strategy.

1. Introduction

Numerical modeling often requires the use of adaptive spatial discretizations to accurately describe the evolution of a process. This is the case of the phase field approach to fracture mechanics. It is a variational approach based on the Griffith's theory of brittle fracture [1] where the sharp crack topology is approximated as bands of non-zero thickness introducing a smooth and continuous scalar field (i.e. the phase field) which represents the damage state of the material. Nucleation and evolution of fractures are therefore determined by the minimization of a two field energy functional, displacement and damage [2, 3]. To this date, the approach has proven its effectiveness and specific formulations have been developed to model different phenomena like asymmetric rupture in traction and compression [4, 5, 6, 7], shear fracture [8, 5, 9], plasticity [10, 11, 12, 13, 14, 15, 16], failure in composite materials [17, 18, 19, 20], cohesive [21, 22], rupture in functionally graded materials [23] and fatigue cracks [24] to cite few.

Since fractures in the solid assume a smeared topology, an intrinsic length scale parameter ℓ is introduced to control the width of the transition zone between the broken and intact portion of the material. As ℓ approaches zero, the sharp crack topology, as well as the Griffith's theory, are recovered in a $\Gamma-$convergence sense [25]. Furthermore, smaller values of ℓ lead to narrow transition zones and therefore, an extremely fine mesh is required to describe and capture correctly the sharp variations of the phase field and the high deformations within the solid. The problematic is exacerbated by the unknown fracture locations. Then, an extremely fine decomposition of the entire domain becomes necessary to obtain accurate solutions at a price of massive computational costs.

To tackle this problem, numerous solutions and optimization strategies have been proposed in the literature. In [26] a predictor-corrector scheme is developed and the mesh is adaptively refined where damage surpasses a fixed threshold. Similarly, a refinement scheme using trimmed hexahedral meshes where additional thresholds are added in order to have a more smooth transition between the refined and unrefined areas of the mesh is proposed in [27]. In [28], the combination of quadtree decomposition and recovery

*Corresponding Author
Email addresses: francesco.freddi@unipr.it (F. Freddi), lorenzo.mingazzi@unipr.it (L. Mingazzi)

based error indicators is used to track automatically the crack trajectory, allowing to perform a local domain discretization. While in [29], a strategy for mesh adaptivity which involves the usage of *h-refined elements* along cracks and *standard elements* in the rest of the domain is investigated. Continuity between refined and unrefined adjacent element is imposed in a weak form via Nitsche's method. Other adaptive mesh refinement methods are presented in [30, 31, 32, 33, 34, 35]. Global/local approaches [36, 37, 38] are also an alternative strategies used to reduce the computational costs of phase field simulations. In [39] the full displacement/damage problem is solved on a local scale using meshes which are dynamically updated during the computation, while dealing with a purely linear elastic problem at the global scale. Coupling of the global/local approach with XFEM to model cracks on the global mesh has been proposed in [40]. Multiscale strategies [41, 42], and implementation of machine learning for the solution of the phase-field problem [43] have also been presented.

In this work, unlike classical refinement methods that rely on error indicators and similarly to [33], where a physically based criterion is adopted, an idea that combines the intrinsic energetic features of the approach together with damage optimal profile extension is considered. The procedure is activated in those areas where the elastic source of damage exceeds a defined threshold. Starting from an initial coarse mesh, adaptivity is limited to the process zone defined by the optimal profile and its neighbourhood, therefore limiting the spreading of refinement. The strategy is implemented both in a global and global/local approach. Recently, it has been demonstrated numerically in [44] that, in accordance with theoretical results [45], the accuracy of the solution is obtained for a certain value of the ratio between the finite element size to the internal length scale parameter. Hence, the refinement procedure is stopped upon reaching a prescribed value of this ratio.

Initially, a global adaptive mesh refinement is employed. From the solution of the global elastic problem, the active area is determined and the mesh adaptive refinement of the corresponding elements is performed [26, 30]. Both the elastic and damage problems are solved on the global refined mesh updated at each iteration of the incremental iterative algorithm. Thereafter, a global/local approach is considered. The elastic problem is solved on the coarse global mesh, and the active area is determined. From the coarse active elements, the local mesh is defined, and the adaptive refinement is performed only at the local scale. Once the local displacement and phase field problems are solved, the damage profile is interpolated back into the global mesh [37, 39], appropriately refined only where the phase field exceeds a fixed threshold. In both the approaches the completely damaged portions of the solid are always subjected to full refinement.

Two different numerical examples are presented in order to illustrate the effectiveness of the proposed strategies. As a comparison, the solution and the computational costs obtained with an almost uniformly refined mesh are considered. Subsequently, the effects of the active zone on the performance and precision of the results is investigated via a parametric analysis.

The paper is organized as follows. In Section 2 a concise overview of the phase field approach is presented. The criterion employed for the refinement procedure is introduced in Section 3 while the refinement strategies and some implementation details, are described in Section 4. The numerical tests are presented in Section 5 whereas the results are illustrated and commented in Section 6. The conclusions of Section 7 complete the paper.

2. Phase field method

In this section the phase field approach is briefly presented. Interested readers can refer to [46] for further details.

Let consider the solid $\Omega \in \mathbb{R}^d$ $(d = 1, 2, 3)$ illustrated in Fig. 1 which contains a crack set $\xi \in \mathbb{R}^{d-1}$. In the variational approach to Griffith's theory for brittle fracture, the total energy functional, which takes into account both the strain energy and the energy dissipated by the formation of cracks within the body, is given by:

$$\Pi(\mathbf{u}) = \int_{\Omega \setminus \xi} \frac{1}{2} \mathbb{C}\mathrm{E}(\mathbf{u}) \cdot \mathrm{E}(\mathbf{u}) \, \mathrm{dx} \quad + \quad G_c \, \mathrm{meas}(\xi) \tag{1}$$

where the first term is the elastic strain energy with $\mathrm{E}(\mathbf{u}) = \nabla^s \mathbf{u}$ the symmetric part of the displacement gradient and the second term represents the fracture energy contribution, proportional to the crack surface

length via the fracture toughness G_c ("meas" refers to the Haussedorf d-1 measure).

The minimization of functional (1) coupled with proper boundary conditions governs the evolution of the fracture process. However, because of the extreme difficulties encountered in the numerical treatise of the sharp approach, a regularization of the fracture energy term is mandatory. To do so, the phase field method approximates the energetic functional in a $\Gamma-$convergence sense via the introduction of a smooth scalar field $\alpha : \Omega \rightarrow [0,1]$, which represents the cohesion state of the material. The value $\alpha = 0$ indicates the material is still intact whereas the value $\alpha = 1$ is assumed where cohesion is fully lost. In addition, a length scale parameter $\ell \in \mathbb{R}^+$ which governs the extension of the transition zone between broken and intact material, is introduced. Accordingly, the functional (1) becomes:

$$\Pi_r(\mathbf{u}, \alpha) = \int_\Omega \left((1-\alpha)^2 + k_r\right) \frac{1}{2} \mathbb{C}\mathrm{E}(\mathbf{u}) \cdot \mathrm{E}(\mathbf{u}) \, \mathrm{dx} \; + \; \frac{3}{8} G_c \int_\Omega \left(\frac{\alpha}{\ell} + \ell ||\nabla \alpha||^2\right) \mathrm{dx} \tag{2}$$

where the quantity $(1-\alpha)^2 + k_r$ has been added to the strain energy term to penalize the fully damaged zones wherein the coefficient k_r is introduced to render coercive the functional Π_r. In the regularized form of the fracture energy, the choice of the first term α/ℓ allows to describe an initial elastic stage, however other choices are possible [47, 48].

In the case of a one-dimensional setup, the damage profile derived from the functional (2), reads

$$\alpha(x) = \left(1 - \frac{|x - x_0|}{D_0}\right)^2 \quad , \quad x \in [x_0 - D_0, x_0 + D_0] \tag{3}$$

where x_0 is the position where $\alpha = 1$, $\alpha = 0$ elsewhere and $D_0 = 2\ell$ the width of the transition zone as illustrated in Fig. 1.

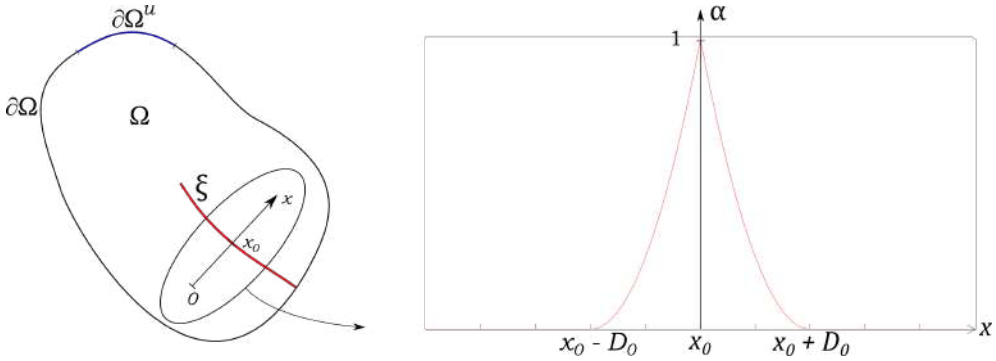

Figure 1: Fracture solid and optimal damage profile.

The minimization of functional (2), which allows to determine the evolution of the fracture within the solid, is given by

$$\min_{(\mathbf{u},\alpha)\in S} \Pi_r(\mathbf{u}, \alpha); \quad S = \left\{(\mathbf{u}, \alpha) \in W^{1,2}\left(\Omega, \mathbb{R}^d\right) \times W^{1,2}(\Omega, [0,1]) \; : \; \mathbf{u} = \bar{\mathbf{u}} \text{ on } \partial\Omega^u\right\} \tag{4}$$

with $\bar{\mathbf{u}}$ the imposed Dirichlet boundary conditions on the portion of the boundary $\partial\Omega^u$.

Differentiating the regularized energy functional of eq. (2) with respect to the displacement field and the phase field, a set of Euler-Lagrange equations is obtained which describes the evolution of the elastic and phase field problem.

$$\begin{cases} \mathrm{div}\ \mathbf{T} = 0 \quad \text{in } \Omega\,, \quad (a) \\ \\ \dfrac{3}{8}\dfrac{G_c}{\ell} - \dfrac{3}{4} G_c \ell \Delta\alpha + Y = 0 \quad \text{in } \Omega\,, \quad (b) \end{cases} \tag{5}$$

with

$$\mathbf{T} = \left((1-\alpha)^2 + k_r\right)\mathbb{C}\mathbf{E}(\mathbf{u}); \quad Y = -(1-\alpha)\,\mathbb{C}\mathbf{E}(\mathbf{u})\cdot\mathbf{E}(\mathbf{u}) \tag{6}$$

the Cauchy's stress tensor and the crack driving force respectively. Lastly, an irreversibility constraint, which avoids healing of the damaged material, is added:

$$\dot{\alpha} \geq 0 \tag{7}$$

At this point, by taking into account the irreversibility condition into the Euler-Lagrange equation which governs the crack evolution, the following Karush-Kuhn-Tucker conditions on the crack evolution process is obtained:

$$\begin{cases} \dfrac{3}{8}\dfrac{G_c}{\ell} - \dfrac{3}{4}G_c\ell\Delta\alpha + Y \leq 0 \quad \text{in } \Omega\,, \\ \dot{\alpha} \geq 0\,, \\ \left(\dfrac{3}{8}\dfrac{G_c}{\ell} - \dfrac{3}{4}G_c\ell\Delta\alpha + Y\right)\dot{\alpha} = 0 \end{cases} \tag{8}$$

The numerical treatment of the phase field approach is typically achieved with an alternate minimization algorithm [49]. In short, the coupled equations (5)a and (8) are solved sequentially until convergence. An elastic problem defined by equation (5)a with fixed phase field values is solved and then the solution of the constrained damage problem (8) is determined at constant displacements. These represent the key problems resolved in the alternate minimization procedure adopted for the phase field problem solution [50].

3. Refinement criterion

In order to obtain accurate solutions which can consistently reproduce the sharp crack topology, the internal length scale parameter has to be assumed small enough leading to thin localization zone [25]. An adequate value of the cell size should be used to capture correctly the steep changes within the phase field and the high displacement gradient [45, 44]. The difficulties are exacerbated since the crack pattern is unknown a priori and extremely fine mesh is required. Consequently, a global refinement would lead to prohibitive computational costs. However, since cracks usually occupy limited portions of the domain, small cell size values are required only in these areas. It is therefore possible to increase the numerical performance via the use of adaptive refinement strategies [51] eventually coupled with a global/local approach [36]. In short, the refined mesh should be able to

- guarantee accurate solution
- anticipate crack initiation
- follow crack propagation
- catch crack bifurcation

Next, the proposed refinement strategies exploit the phase field features: an energetic threshold must be exceeded to activate the damage phenomena and the extension of the process zone is determined by the optimal profile of (3). Element refinement is stopped upon reaching a prescribed cell size to internal length scale parameter ratio. The employed criterion is presented below. Determination of the area involved in refinement will be discussed in Section 4.

3.1. Energy based criterion

The active regions of the domain, where damage occurs, are determined via an energetic criterion. In the areas where the material is intact, i.e. $\alpha = 0$, a simplified version of eq. (8)a determines fracture nucleation if

$$\frac{3}{8}\frac{G_c}{\ell} - \mathbb{C}\mathbf{E}(\mathbf{u})\cdot\mathbf{E}(\mathbf{u}) \leq 0\,. \tag{9}$$

Then, the following criterion is adopted

$$\beta_1 \cdot E_{rif} - \mathbb{C}\mathbf{E}(\mathbf{u}) \cdot \mathbf{E}(\mathbf{u}) < 0 \tag{10}$$

being $E_{rif} = \frac{3}{8}\frac{G_c}{\ell}$ the elastic threshold and $\beta_1 \leq 1$ a coefficient adopted to anticipate the refinement procedure and to modulate the size of the predicted active zone. This criterion permits to identify the areas where the damage will develop and follow the fracture paths with localized deformations.

Criterion (10) is tested in a simple 2D setup of a notched bar in traction. Fig. 2 reports the normalized elastic energy and phase field profile at different iterations of the minimization process. Both graphs refer to the bar portion affected by damage along an horizontal line placed in mid-height. Crack nucleates as the elastic threshold E_{rif} is exceeded by the elastic source $E_n = \mathbb{C}\mathbf{E}(\mathbf{u}) \cdot \mathbf{E}(\mathbf{u})$ (iteration 4, 10). In the iteration process E_n increases near x_0 where damage presents the maximum value whereas in the remaining areas decreases (iterations 37, 38). Lastly, once the phase field assumes value 1 near x_0, the localization process starts. Finally, $E_n > E_{rif}$ occurs only where cohesion is fully lost and the phase field assumes the optimal profile graph of (3) (iterations 39, 44). Definitely, criterion (10) correctly catches damage initiation and evolution during the iteration process.

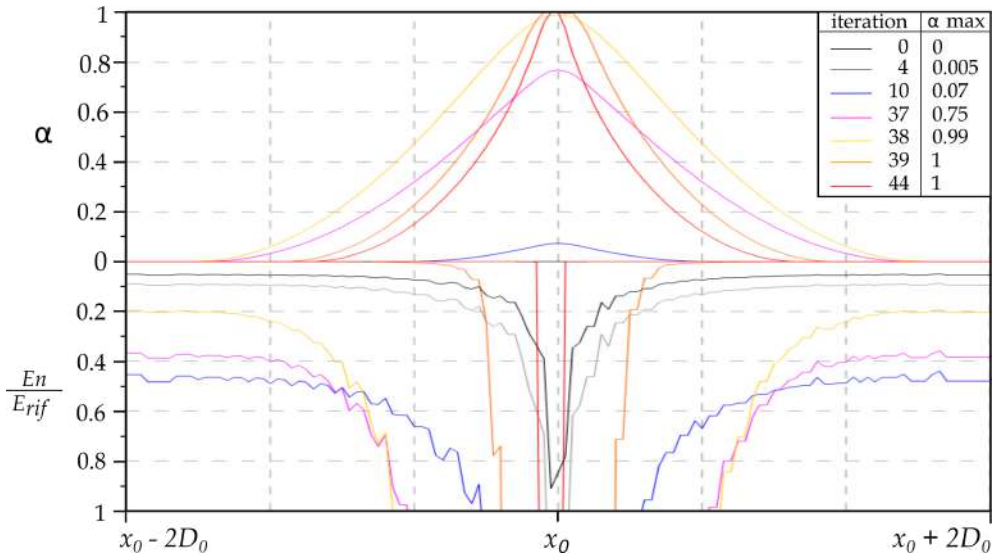

Figure 2: Normalized energy profiles (bottom side) and the respective damage profiles (upper side) at subsequent iterations. Iteration number 44 corresponds to the last iteration in which convergence is achieved.

4. Refinement strategies

In this section the developed global and global/local refinement strategies are presented. In both cases the initial step is common: the solid is discretized with a global coarse mesh with element size h_{coarse}. The solution obtained with an almost uniform refinement of the areas where cracks are expected to develop is considered as reference (Global displacement - Global phase field (Gu - Gα)).

4.1. Adaptive Global displacement - Adaptive Global phase field (AGu - AGα)

The following main steps are performed in the global adaptive refinement technique at each iteration of the alternate minimization algorithm

1 - the elastic problem is solved on the global coarse mesh;
2 - active elements are determined;
3 - adaptive refinement of the active elements is performed;
4 - elastic and phase field problems are solved on the global adaptive refined mesh.

The procedure is graphically represented in Fig. 3. Step 1 is performed only if no active element is detected whereas steps 2, 3 and 4 are repeated at each iteration of the alternate minimization algorithm until convergence. However, if the active elements do not change between two subsequent iterations only the steps 2 and 4 are performed:

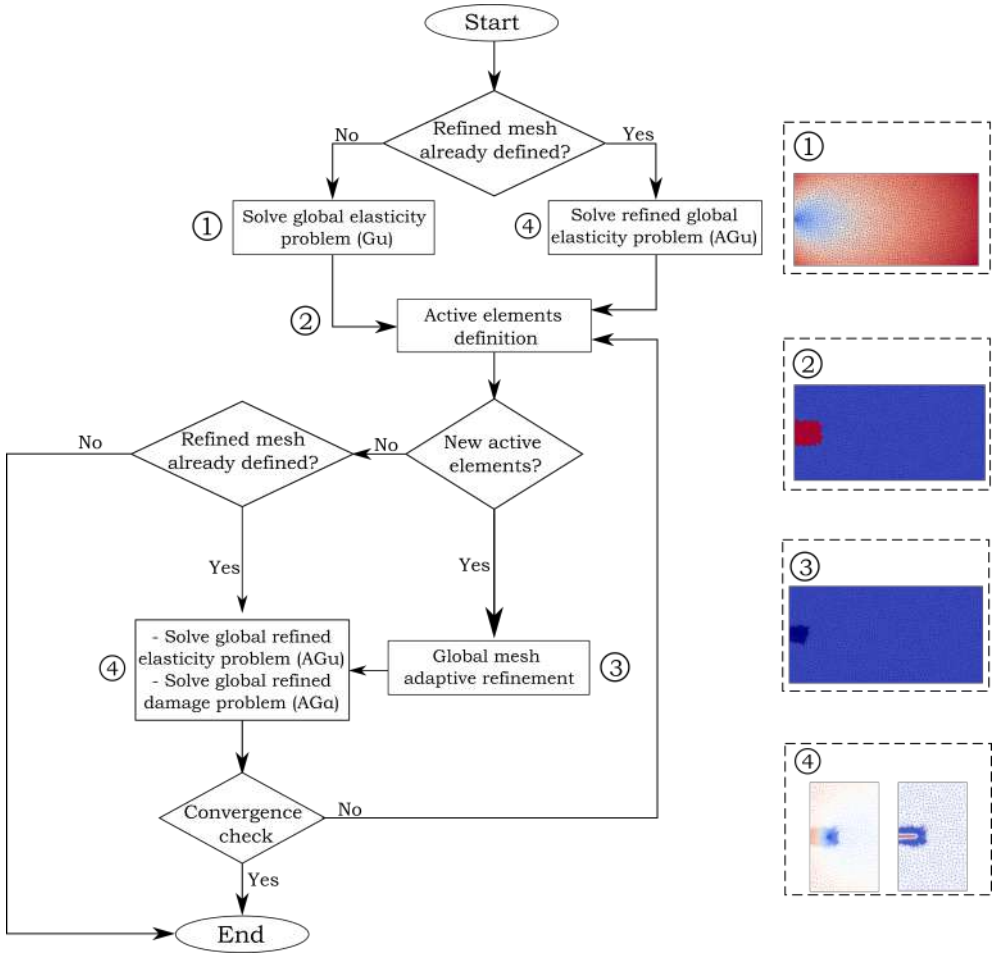

Figure 3: Time step flowchart of the AGu - AGα strategy.

Additional details concerning steps 2 and 3 are given.

Step 2: Definition of the active elements to be refined

The procedure to define the portion of the mesh to be refined is described in short and is graphically depicted in Fig. 4. Firstly, the active elements el_{active}, where the inequality (10) is satisfied in at least a single gauss point, are identified. Secondly, the transition zone between damaged and undamaged state of the material, governed by the internal length scale parameter ℓ, is included in the refinement process. Specifically, the elements el_{add} which are within a distance $r_{in} = \beta_3 \ell$ to el_{active} are detected. The coefficient $\beta_3 \geq 2$ permits to extend the refinement process according to the optimal profile extension of eq. (3).

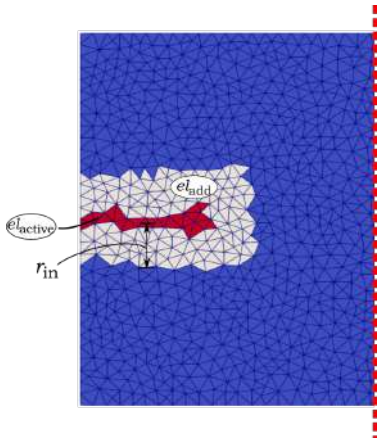

Figure 4: Set of elements on the global mesh for the global refinement procedure: el_{active}, el_{add}

Step 3: Adaptive refinement

Once the set of elements el_{active} and el_{add} are determined at step 2 (see Fig. 5a), the adaptive refinement can be performed. A smooth transition from coarse elements to the highly refined portion of the fully damaged areas has to be guaranteed to avoid excessive mesh distortions. At the same time the refinement is deepened in the evolving and fully damaged zones.

First, the elements el_{active} and el_{add} are h-refined a number of times equal to Ref_{add}. This provides the first set of refined elements localized in the damaged and transition zones. During the refinement process, child elements assume the same definition of the parent element as shown in Fig. 5b. Eventually, only the active elements el_{active} are refined again a number of times equal to Ref_{active}. However, a distinction is required within the set of active elements. Where damage is fully developed and is no more evolving, in order to limit the refinement in the zone, the elements el^{old}_{active} are fully refined only where damage exceeds a value threshold α_s. Analogously, full refinement is performed in the new active elements el^{new}_{active} where phase field is increasing. Therefore, for the second refinement process the following conditions are considered as illustrated in Fig. 5c:

- the new active elements determined at the current time step el^{new}_{active} are refined Ref_{active} times;
- the old active elements el^{old}_{active}, with a phase field values α greater than a set damage threshold α_s, are refined Ref_{active} times only if $\alpha \geq \alpha_s$;

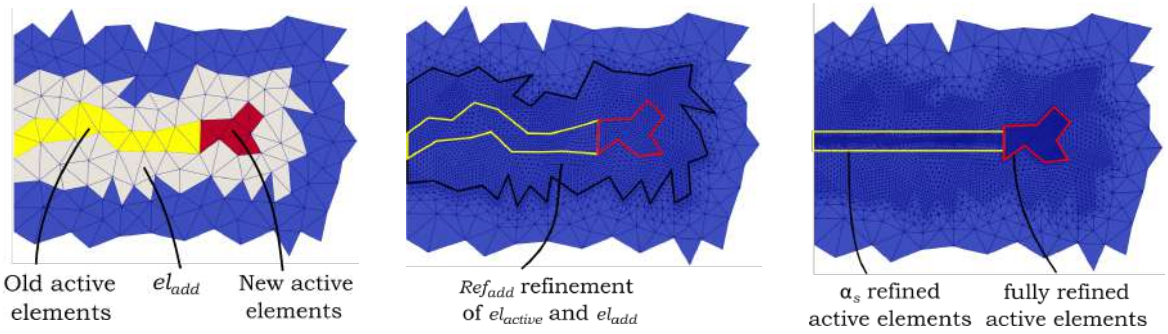

a) b) c)

Figure 5: Refinement of the active elements: a) old and new active elements, b) first refinement process, c) final refinement of the active and fully damaged zones.

A coarsening effect in the neighborhood of the fully damaged zones with the phase field that is no more evolving is introduced as illustrated in Fig. 5c. Moreover, this strategy results in a mesh with elements of

almost constant size in the process zone minimizing the effects on the fracture pattern that can occur in the case of mesh with a rapid size variation. Finally, in order to implicitly keeps into account the irreversibility of refinement in case of mechanical unloading the set of el^{old}_{active} with child elements having $\alpha \geq \alpha_s$ are maintained in the list of el_{active}.

4.2. α_s adaptive Global displacement - Adaptive Local displacement - Adaptive Local phase field (aGu - ALu - ALα)

In the global/local refinement strategy, at each iteration of the alternate minimization algorithm, the elastic problem is firstly solved at global level, subsequently the elastic and the damage problems are solved at local scale. The local mesh is discretized and refined adopting a strategy similar to the one adopted for the global refinement strategy. At the global level instead, a specific refinement is performed to encapsulate the kinematics of the fully damaged region. The following main steps, graphically summarized in Fig. 6, are performed:

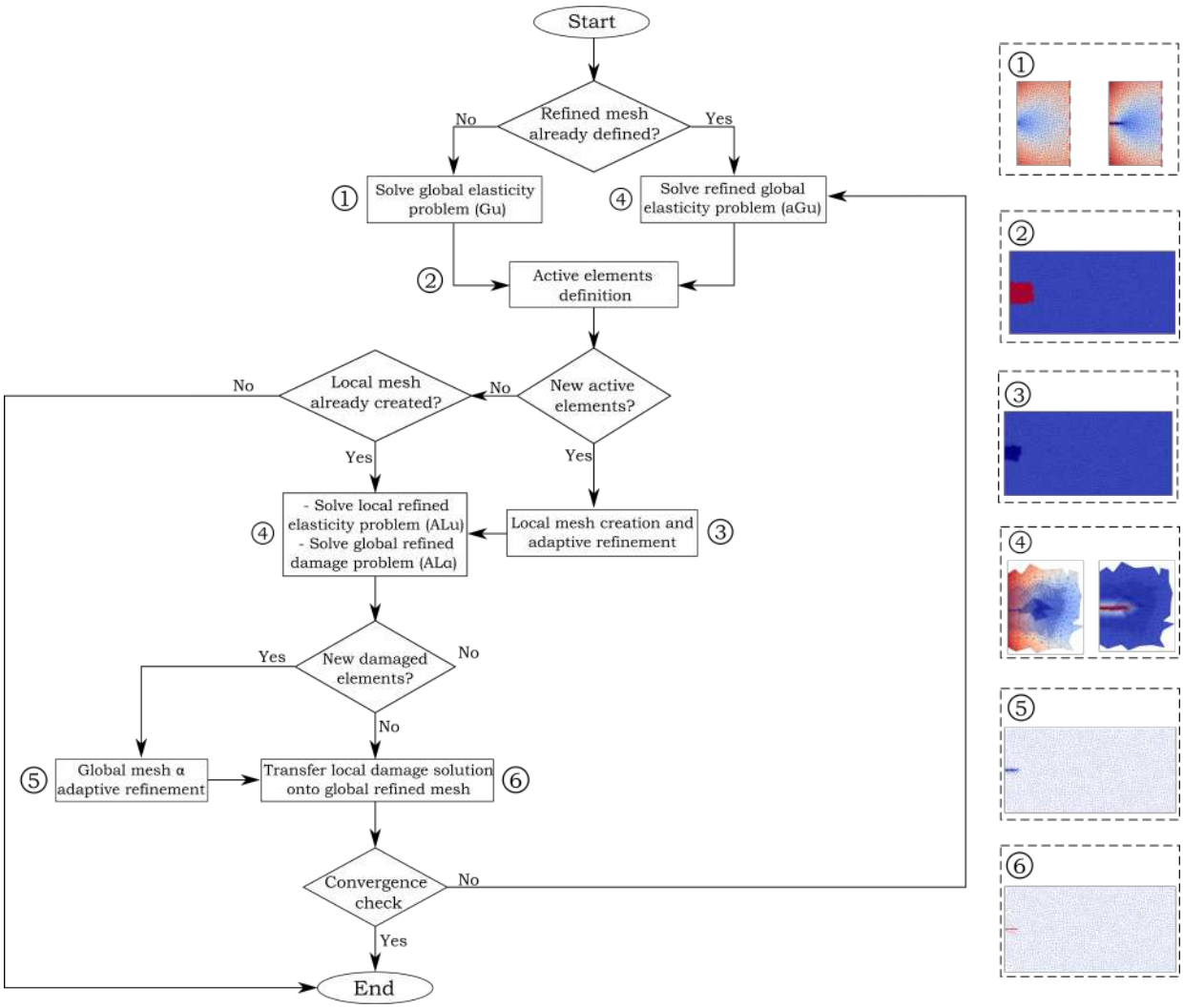

Figure 6: Time step flowchart of the aGu - ALu - ALα strategy.

1 - the elastic problem is solved on the global mesh;

2 - active elements are determined;

3 - the local mesh is created and the active elements are adaptively refined;

4 - the local problems are solved: the elastic solution on the global mesh is assumed as a boundary condition for the local elastic problem;

5 - selective refinement of global mesh;

6 - interpolation onto the global mesh of the local phase field solution

At each iteration of the alternate minimization algorithm steps 1-6 are repeated. If the active elements do not change in the iteration process, the local mesh is not redefined and therefore step 3 is skipped. Moreover, if no new damaged elements where $\alpha \geq \alpha_s$ are found, step 5 is also skipped. Being Step 2 equivalent to step 2 of 4.1 and step 4 standard, only details concerning steps 3, 5 and 6 are given.

Step 3: Definition of the coarse local mesh and local problem definition

Here, the local coarse mesh has to be defined. In addition to the elements identified in step 2 of the global refinement procedure, a spare set of finite elements el_{out} surrounding el_{add} is determined by use of an additional distance parameter r_{out} as illustrated in Fig. 7. Now, the local mesh is defined by $el_{active} \cup el_{add} \cup el_{out}$. In particular, the outer boundary $\partial\Omega_L^u$ of the local mesh will not be interested by refinement and coincide with the elements of the global coarse mesh, automatically recovering the continuity between the two meshes and permitting a simplified boundary condition imposition. In fact, the displacement field determined by the solution of the elastic problem on the global mesh is imposed on the outer contour of the local mesh. For the simulations r_{out} has been chosen equal to $\beta_2 h_{coarse}$ with $\beta_2 \geq 1$ to always ensure the presence of one coarse outer element. Afterwards, the local mesh refinement process is performed following the passages of step 3 of the global strategy presented in 4.1.

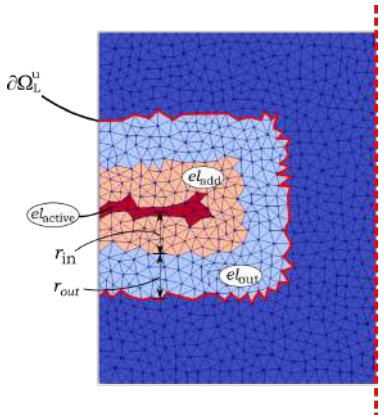

Figure 7: Set of elements on the global mesh for the global/local refinement procedure: el_{active}, el_{add}, el_{out}

Step 5: Selective refinement of global mesh (α refinement)

The obtained local solution is transferred onto the global mesh specially refined in the fully damaged region. In fact, too coarse mesh leads to unrealistic solid behavior as outlined in Fig. 8a where a simple interpolation of the local damage field onto the global coarse mesh has been performed. In fact, the phase field maps of Fig. 8a is unable to replicate the behaviour of a fractured solid. Alternatively, X-FEM are adopted to simulate the kinematic of a crack [40]. Here, an extremely localized refinement of the global mesh is performed. At each iteration, the position on the local fine mesh of the set of elements el_α where $\alpha \geq \alpha_s$ with $\alpha_s < 1$, is determined. Any active element on the coarse mesh which contains an element of the set el_α is refined. This selective refinement procedure permits to correctly reproduce the kinematics of a fully damaged solid with a limited increment of the dofs of the global mesh as reported in the Fig. 8b and to keep the initial idea of a regularised problem that is the basis of the phase field approach.

In practice, the definition of the refined global mesh is done whenever a new element in the local mesh exceeds α_s. Within the coarse mesh, the element containing the centroid of the smaller elements el_α is refined a number of times equal to Ref_{in}. Moreover, the refinement is performed such that the compatibility condition between adjacent elements is maintained and no hanging nodes are introduced. The presence of

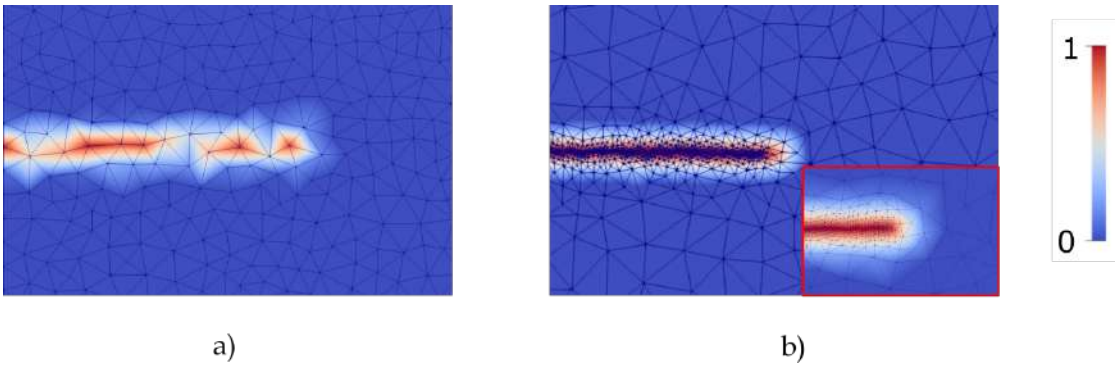

Figure 8: Interpolation of the local damage profile on the global mesh: a) unrefined mesh; b) α_s adaptively refined mesh

hanging nodes needs specific treatment, see the Finite element Library Deal.II [52] for an elegant effective procedure.

Step 6 - Local to global solution interpolation

The local damage field α is interpolated onto the global mesh, obtaining a global phase field α_G which correctly reproduce the macroscopic discontinuity due the presence of a crack.

5. Tests setup

The performances of the refinement techniques are compared into two representative examples. The adopted coefficient values are reported in Table 1. Furthermore, in the first example the coefficients α_s, β_1, β_2 and β_3 are varied to perform a sensitivity analysis assessing the impact on the accuracy and computational costs of the optimization strategies.

Coefficient	value
α_s	0.9
β_1	1
β_2	1
β_3	2
Ref_{in}	4
Ref_{add}	2
Ref_{active}	Ref_{in} - Ref_{add}

Table 1: Optimization coefficient initial values

The different refinement strategies summarized in Tab. 2 have been implemented in specific codes developed using the open access FEniCS library [53] for finite elements and PETSc [54] for linear algebra operations, including bound-constrained solvers. All the implementation details will be object of a forthcoming paper [55]. In the numerical simulations, the domain is discretised with an unstructured triangular mesh with linear shape functions for both displacements and damage fields. The mesh refinement process is performed via the `refine` module present in the FEniCS library. This refinement procedure automatically subdivide the chosen elements into smaller ones. Moreover, their closest elements are modified accordingly to prevent the creation of hanging nodes. In order to achieve optimal performance in the evaluation of the distances between the centroid of two finite elements, the SciPy cKDTree [56] has been used. In particular, the `query_ball_point` method permits a fast evaluation of the distance between two given points. The

tests were performed using a single core of the INTEL XEON E7-8880v4 2.2GHz 22c with 128 GB of memory, provided by the High Performance Computing server cluster of the University of Parma.

Type	Global $\mathbf{u}$	Global α	Local $\mathbf{u}$	Local α	Global mesh	Local Mesh
1 - G$\mathbf{u}$-Gα	✓	✓	-	-	U	-
2 - AG$\mathbf{u}$-AGα	✓	✓	-	-	A	-
3 - aG$\mathbf{u}$-AL$\mathbf{u}$-ALα	✓	-	✓	✓	a	A

Table 2: Summary of the refinement strategies adopted in the tests. The symbols: "✓" indicates the problem is solved at each iteration; "-" indicates the problem is not solved or the local mesh not defined, "a" indicates that the mesh is refined only where the damage field is above α_s, "A" indicates that the mesh is adaptively refined only in active regions, "U" indicates that the mesh is uniformly refined.

5.1. Stable crack propagation

The stable crack propagation surfing problem illustrated in [57, 58] has been studied. A rectangular domain $\Omega = [0,\ \mathrm{L}] \times [-\mathrm{H}/2,\ \mathrm{H}/2]$ is considered. A steadily advancing crack at constant speed v along the central horizontal line of the domain is obtained. The displacement, applied to the whole external boundary as indicated in Fig. 9, allows for the stress intensity factor K_I to control the load intensity and reads

$$\begin{aligned}\mathbf{U}(x, y, \mathrm{t}) &= \bar{\mathbf{U}}(x - v\mathrm{t}, y) \\ &= \frac{K_I}{2\mu}\sqrt{\frac{r}{2\pi}}\left(\frac{3-\nu}{1+\nu} - \cos\vartheta\right)(\cos(\vartheta/2)\mathbf{e}_1 + \sin(\vartheta/2)\mathbf{e}_2) \quad \text{on} \quad \partial\Omega_{\mathbf{u}}\end{aligned} \tag{11}$$

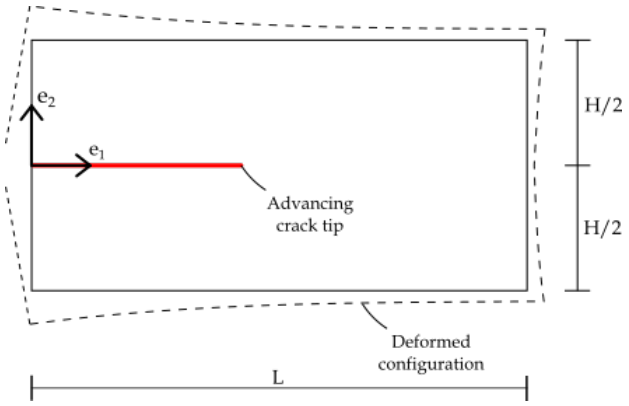

Figure 9: Surfing condition test setup

where μ is the shear modulus, ν is the Poisson coefficient, t is the time, (r, ϑ) are the polar coordinates centered at the advancing crack tip, $(\mathbf{e}_1, \mathbf{e}_2)$ represent the cartesian unit vectors and $r = \sqrt{(x - v\mathrm{t})^2 + y^2}$.

The rectangular domain has dimensions $\mathrm{L} = 2\ mm$, $\mathrm{H} = 1\ mm$ whereas the parameters for the displacement expression have been taken equal to $K_I = 1\ MPa\sqrt{mm}$, $v = 1\ mm/s$. The material parameters are: Young's modulus $E = 1\ MPa$, Poisson's ratio $\nu = 0.3$, phase field characteristic length $\ell = 0.02\ mm$, material fracture toughness $G_c = 1\ N/mm$. An unstructured mesh with triangular elements has been used. The reference solution is obtained with a uniformly refined mesh in the central portion of the solid by a height equal to 5ℓ since the crack pattern is known a priori with cell size to internal length ratio equal to $h/\ell = 1/8$. For the adaptive strategies a coarse starting mesh has been adopted as reported in Fig. 10 with $h = 2\ell$. In the simulations it has been assumed $\mathrm{t} \in [0, \mathrm{T}]$, with $\mathrm{T} = 2$ seconds.

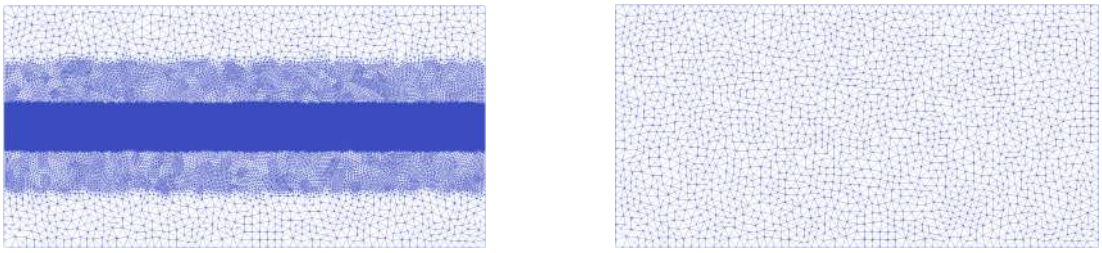

a) b)

Figure 10: Initial mesh: a) case Gu-Gα; b) cases AGu-AGα, aGu-ALu-ALα

5.2. Abrupt crack propagation and branching

A plate with three different pre-existing cracks under biaxial traction condition according to Fig. 11a is studied similarly to [29]. The crack tips coordinates are listed in Table 3. Here, the pre-existing cracks lead to initial localized active zones where damage nucleates, allowing to examine the evolution of the problem in more limited refined areas. In this case the damage patterns are unknown, and fractures propagate and branch brutally.

The dimensions of the domain have been assumed equal to L = H = $2mm$. The material parameters were: Young's modulus $E = 210000MPa$, Poisson's ratio $\nu = 0.3$, phase field characteristic length $\ell = 0.03mm$, material fracture toughness $G_c = 0.075N/mm$. An initial unstructured coarse mesh with triangular elements has been considered for refinement strategies as illustrated in Fig. 11b with $h = 2\ell$. An almost uniform refinement has been performed for case Gu-Gα up to $h/\ell = 1/8$. The applied displacements are $\bar{u} = \bar{u}_x = \bar{u}_y = 0.003\,t\ mm$ being $t \in [0, 1]$ a time like parameter.

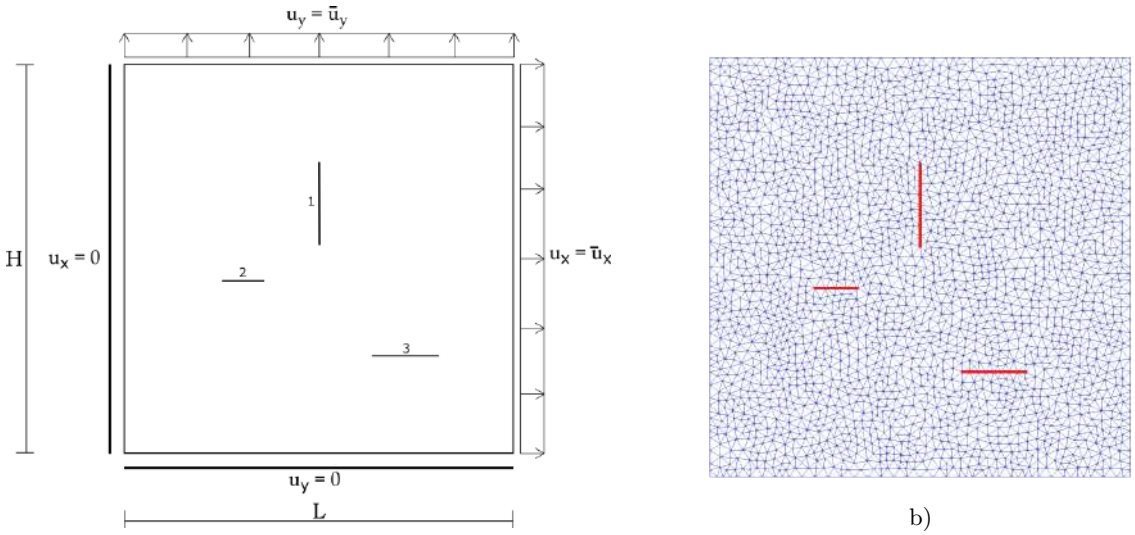

a) b)

Figure 11: Unstable test setup: a) geometry and boundary conditions; b) Initial coarse mesh

6. Results

The results of the numerical examples presented in Section 5 are illustrated.

Crack	Tip 1	Tip 2
1	(1, 1.1)	(1, 1.5)
2	(0.5, 0.9)	(0.7, 0.9)
3	(1.2, 0.5)	(1.5, 0.5)

Table 3: Crack tip coordinates. The origin of the system coordinates is assumed at the left bottom corner of the plate

6.1. Stable crack propagation test

In this test, the crack propagates horizontally at constant speed as depicted in Fig. 9. Accordingly, the fracture energy grows linearly as crack propagates according to Griffith theory [59, 58]. The values of approximated fracture energy obtained from the refinement strategies are compared with the theoretical ones and those obtained from the reference test. A correction factor that depends on the ratio h/ℓ has to be taken into account in order to remove the additional energetic contribution given by the fully damaged finite element band [46, 60]. Moreover, a second contribution due to the presence of the crack tip has been considered according to [61]. Therefore, the effective fracture energy $\Pi_{\text{frac, eff}}$ of Fig. 12a is obtained according to

$$\Pi_{\text{frac, eff}} = \Pi_{\text{frac}} \cdot \frac{1}{\left(1 + \frac{3h}{8\ell}\right)} \; - \; \frac{3}{8} G_c \ell \tag{12}$$

where Π_{frac} is the value of the approximated fracture energy obtained from FEM simulations. In Fig. 12a the values of $\Pi_{\text{frac, eff}}$ obtained with the refinement techniques are in good agreement with the benchmark test as well as with the theoretical values for a crack steadily propagating at a speed equal to v.

The load-time curves are reported from Fig. 12b. There is a satisfactory agreement between the reference test and the solutions obtained with the refinement approaches. From this result it can be mentioned that the refined global mesh of the aGu-ALu-ALα, which is performed only where the phase field is above the threshold α_s, permits to consistently reproduce at a global scale the crack pattern interpolated from the local solution.

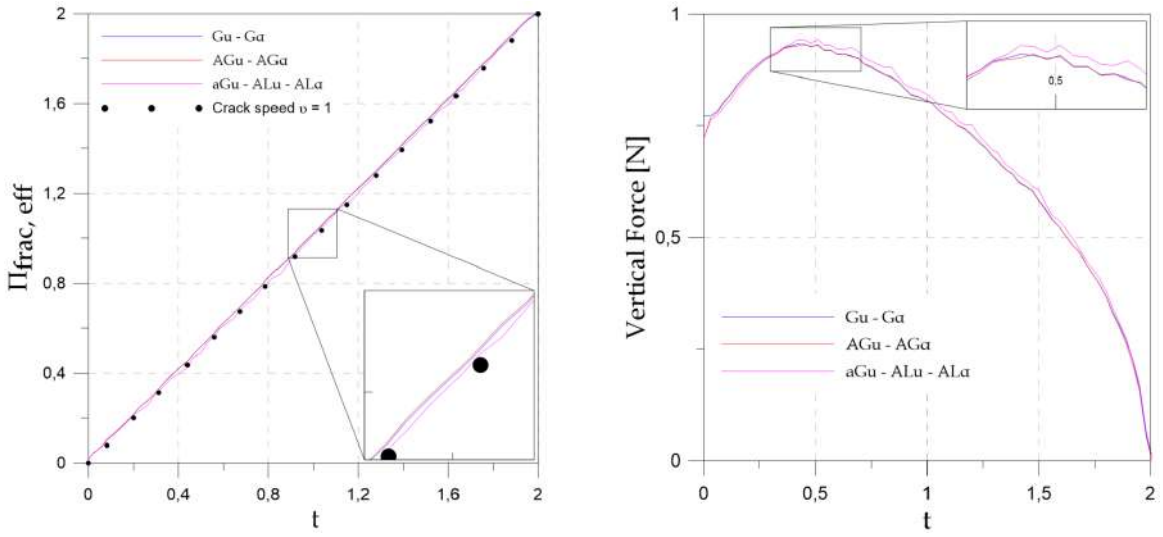

a) b)

Figure 12: a) Evolution of the effective fracture energy ; b) Load-time curves

The effectiveness of the strategies is also highlighted in Fig. 13, where the damage profiles obtained from the three discretization strategies, plotted along a direction orthogonal to the crack, correctly approximate

the theoretical optimal profile.

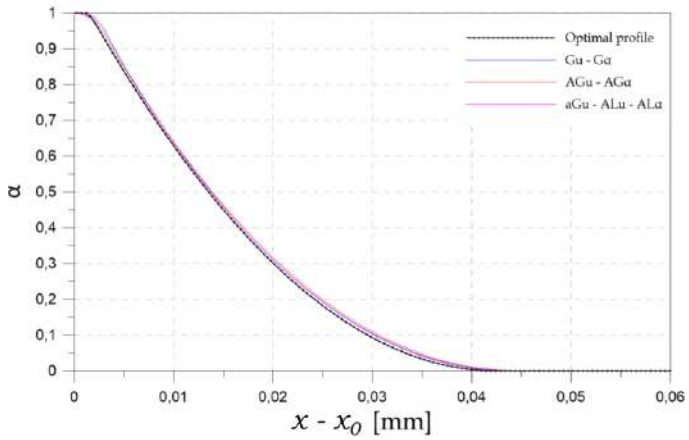

Figure 13: Phase field profiles for each strategy being x_0 the position of the cracks.

The global and local meshes are reported in Fig. 14 at different time steps. In the AGu-AGα case, the refinement follows the evolution of the process, limiting the zone characterized by a fine mesh where the material is completely damaged and including the entire transition zone. In the aGu-ALu-ALα strategy the global refinement has the unique purpose of allowing the elastic solution to reproduce a discontinuity due to the presence of the completely damaged zone. In the local mesh reported in Fig. 14g the line surrounding the damage profiles represents the position where the phase field assumes value $\alpha = 0$. The local mesh is obtained such that the transition zone between broken and intact material is contained within the refined elements of the mesh (el_{active} and el_{add}), while the outer elements (el_{out}) are included to maintain the continuity between the local and global meshes.

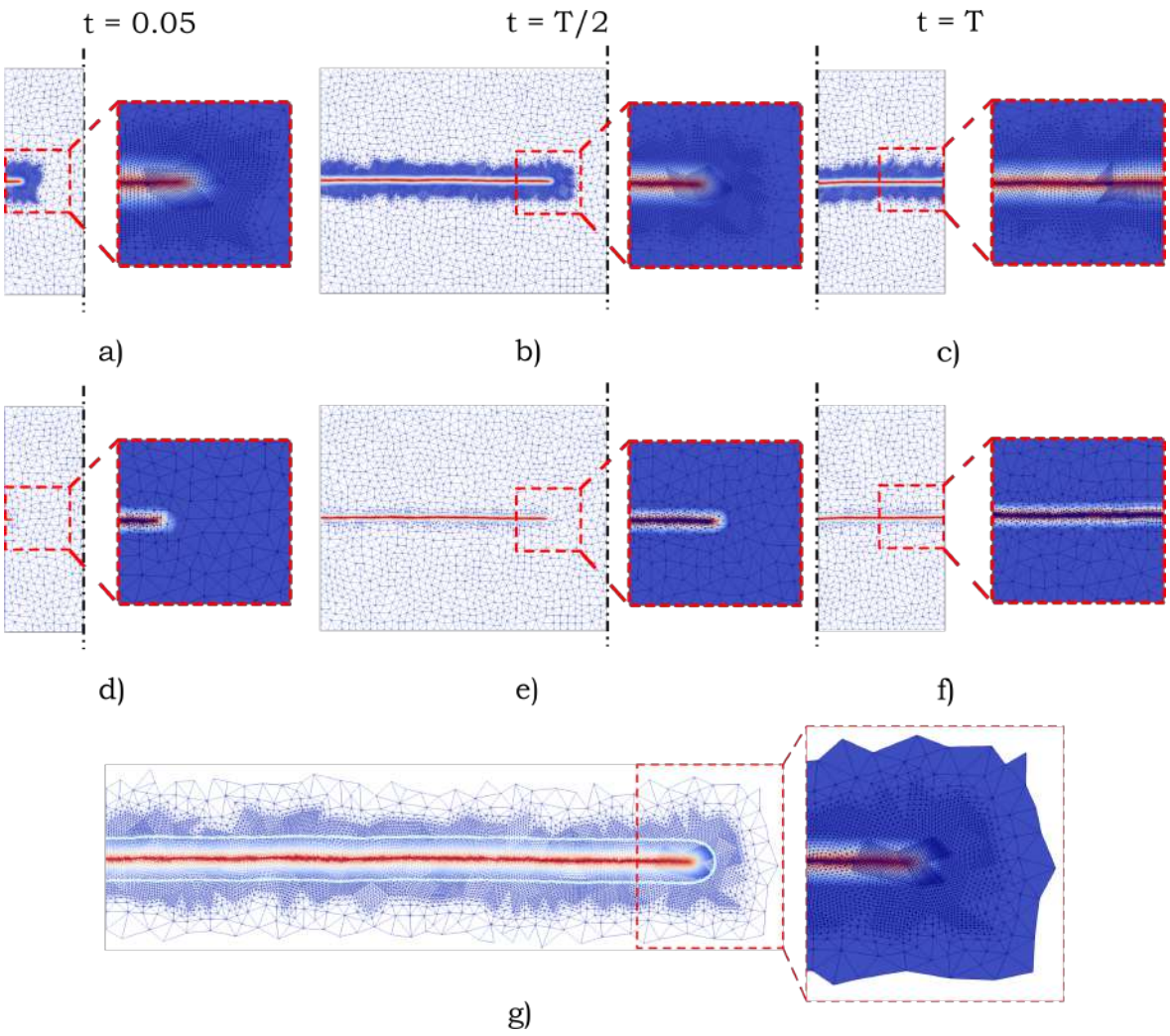

Figure 14: Adopted meshes at different time steps. Time t = T refers to the time step when the full crack has developed within the domain. a), b), c) Global meshes used for AGu-AGα. d), e), f) Global mesh used for aGu-ALu-ALα. g) Local mesh used for aGu-ALu-ALα at t = T/2

Now, the computational costs of the various procedures are investigated. Figs. 15 and 16 report the average time per iteration and the cumulative time for the elastic and damage problems of the alternate minimization algorithm respectively. For almost uniform global refinement Gu-Gα the time is practically constant (small fluctuations are due to access at share resources of the node). A clear time reduction occurs if an adaptive refinement strategy is used as outlined in Fig. 15a. At the same time, the overall time depicted in 15b reduces of one order of magnitude. The aGu-ALu-ALα strategy has the best performance. The same analysis is performed for the damage problem solution in Fig. 16. A consistent reduction of computational cost is observed in passing from Gu-Gα to adaptive strategies. The aGu-ALu-ALα presents the lower overall time even if the average cost per iteration is similar to the previous two cases. This is due to more limited number of iterations performed in the alternate minimization algorithm to reach convergence at each time step.

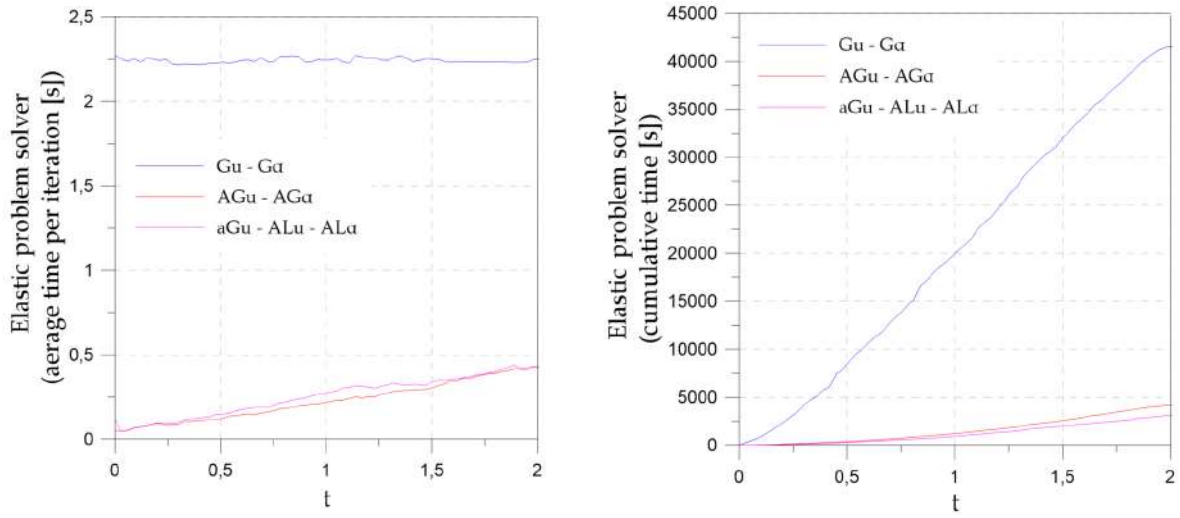

a) b)

Figure 15: Elastic solver time: a) average time per iteration b) cumulative time

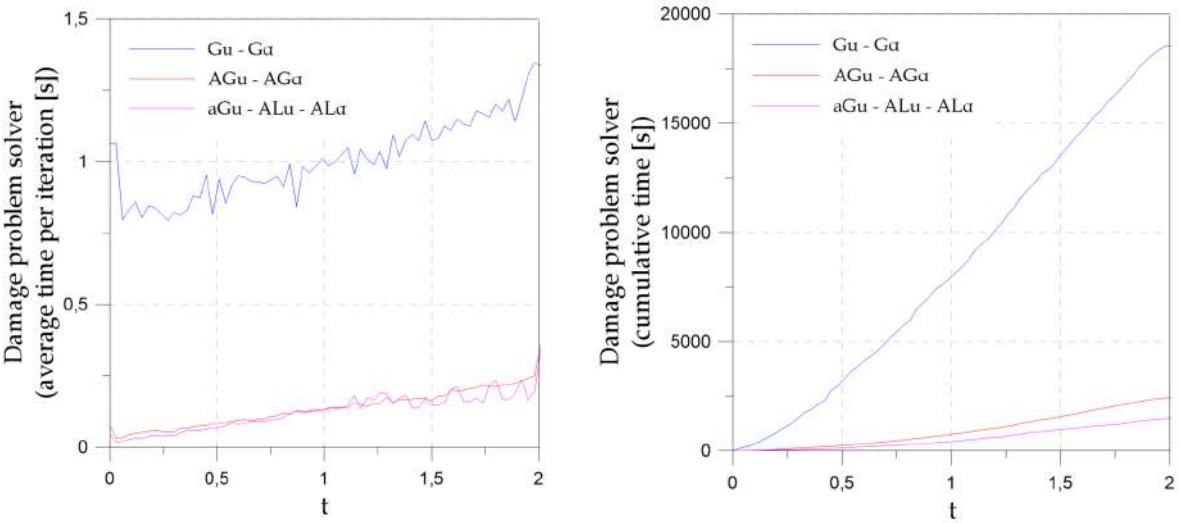

a) b)

Figure 16: Damage solver time: a) average time per iteration b) cumulative time

Fig. 17 shows the degrees of freedom (dof) for a) displacement problem and b) damage problem as a function of time. The computational costs of Fig. 16 are strictly correlated with problem size. The adaptive refinement coupled with the global/local strategy leads to an overall smaller dimension of the displacement and phase field problems, with the number of degrees of freedom growing linearly with the crack advancement.

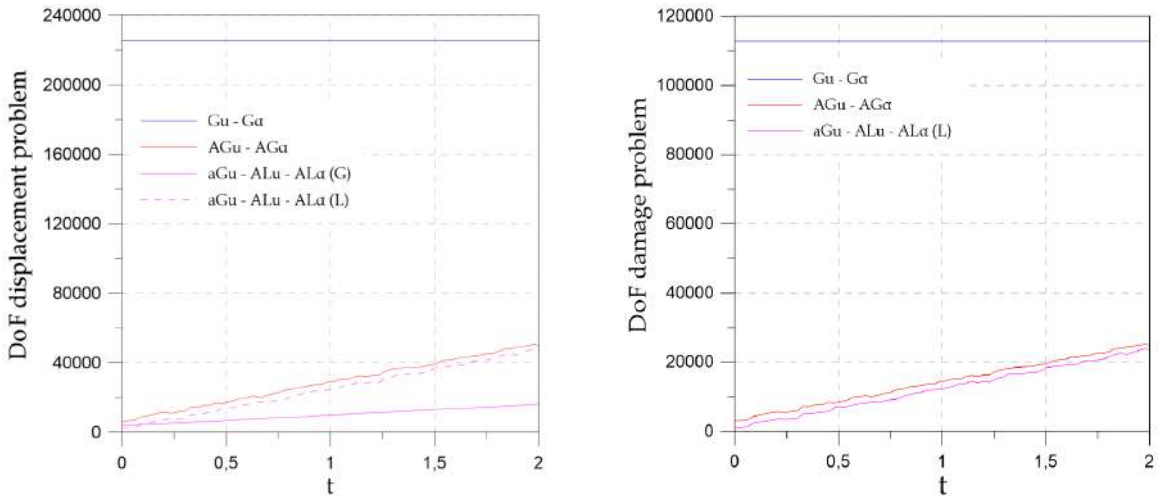

a) b)

Figure 17: Degree of freedom: a) elastic ploblem b) damage problem

The total computational time and the corresponding percentage reduction in the required time to perform the complete simulation for the different optimization procedures compared against the reference test is reported in Tab. 4. Finally, the values of the initial and final degrees of freedom for each optimization procedure are also reported in Tab. 5. Due to the small size of the problems that are solved, computation time drastically reduces. The global/local strategy is $\sim 30\%$ quicker than the global one.

Type	Total computational time [s]	Time reduction (%)
1 - G**u**-Gα	60056	-
2 - AG**u**-AGα	6575	88%
3 - aG**u**-AL**u**-ALα	4552	92%

Table 4: Stable crack propagation test: total computational time and the corresponding percentage reduction in the required time to perform the complete simulation for the different optimization procedures compared against the reference test.

Type	Initial DoF **u**	Initial DoF α	Final DoF **u**	Final DoF α
1 - G**u**-Gα	225468	112734	225468	112734
2 - AG**u**-AGα	6316	3158	49598	24799
3 - aG**u**-AL**u**-ALα	4126 (G) - 2280 (L)	1140 (L)	21256 (G) - 49890 (L)	24945

Table 5: Degree of freedom of the various optimization procedures at the beginning and at the end of the simulation.

6.2. Stable crack propagation - refinement parameter tests

The effects of the refinement parameters $\beta_1, \beta_2, \beta_3, \alpha_s$ on the accuracy of the solution and on the computational costs are investigated. For each parameter value a plot reporting the evolution of the effective fracture energy, the force, average time per iteration and the cumulative computation time is given. In addition, a Table resuming the Dof at the beginning and at the end of the simulation is reported.

- *Reference energy parameter* β_1

Now, the parameter β_1 of eq. (10) affecting the value of the reference energy and crucial to determine the active elements within the mesh is varied. The parameter has been set equal to $\beta_1 = \{0.5, 0.75, 1\}$; lower values lead to a larger number of active elements and therefore to a wider active area.

The influence in term of precision and computational costs of the value of β_1 is rather limited for both the global and global/local strategies. In fact, the adaptively refined zone depicted in Fig.18, where the refined zone for AGu-AGα and aGu-ALu-ALα for different values of the β_1 parameter are reported, are similar for all cases. As a consequence, the fracture energy and the force-time plots show almost equal values. $\beta_1 = 0.5$ leads to a small increment of dof (see Table 6) and therefore to additional computational time for the solution of the elastic and damage problems as shown in Figs. 19, 20.

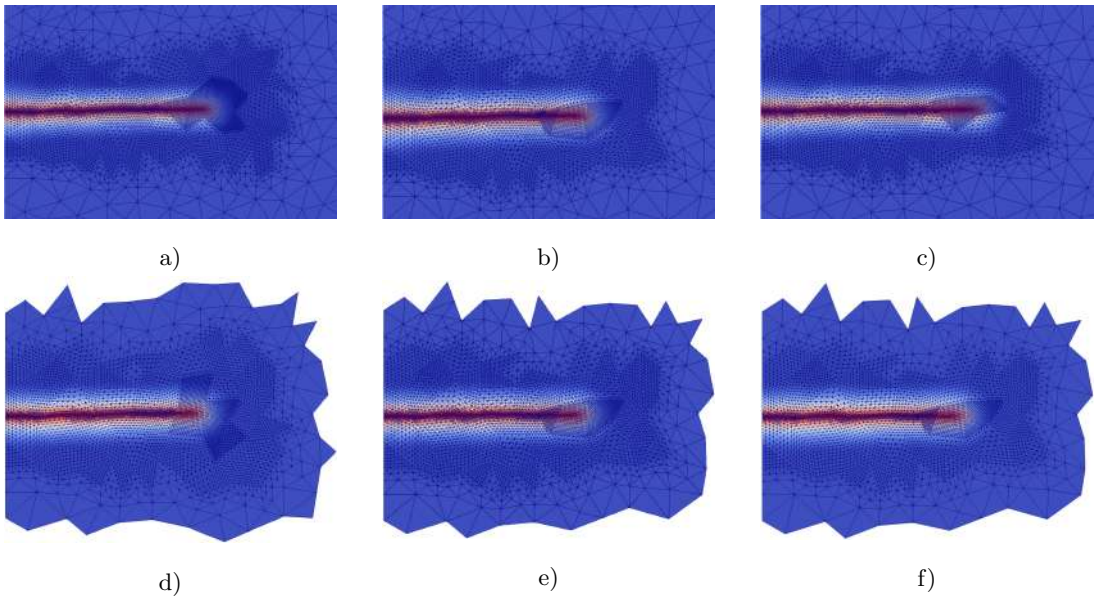

Figure 18: Adaptively refined zone for AGu-AGα and aGu-ALu-ALα for different values of β_1. AGu-AGα: a) $\beta_1 = 0.5$, b) $\beta_1 = 0.75$, c) $\beta_1 = 1$ aGu-ALu-ALα: d) $\beta_1 = 0.5$, e) $\beta_1 = 0.75$, f) $\beta_1 = 1$

Type	Initial DoF $\mathbf{u}$	Initial DoF α	β_1	Final DoF $\mathbf{u}$	Final DoF α
1 - G$\mathbf{u}$-Gα	225468	112734	-	225468	112734
2 - AG$\mathbf{u}$-AGα	6316	3158	0.5	53246	27215
			0.75	52954	26477
			1	49598	24799
3 - aG$\mathbf{u}$-AL$\mathbf{u}$-ALα	4126 (G) - 2280 (L)	1140 (L)	0.5	21256 (G) - 47122 (L)	23561
			0.75	21256 (G) - 46470 (L)	23235
			1	21256 (G) - 45006 (L)	22503

Table 6: Degree of freedom of the various optimization procedures at the beginning and at the end of the simulation for different values of β_1.

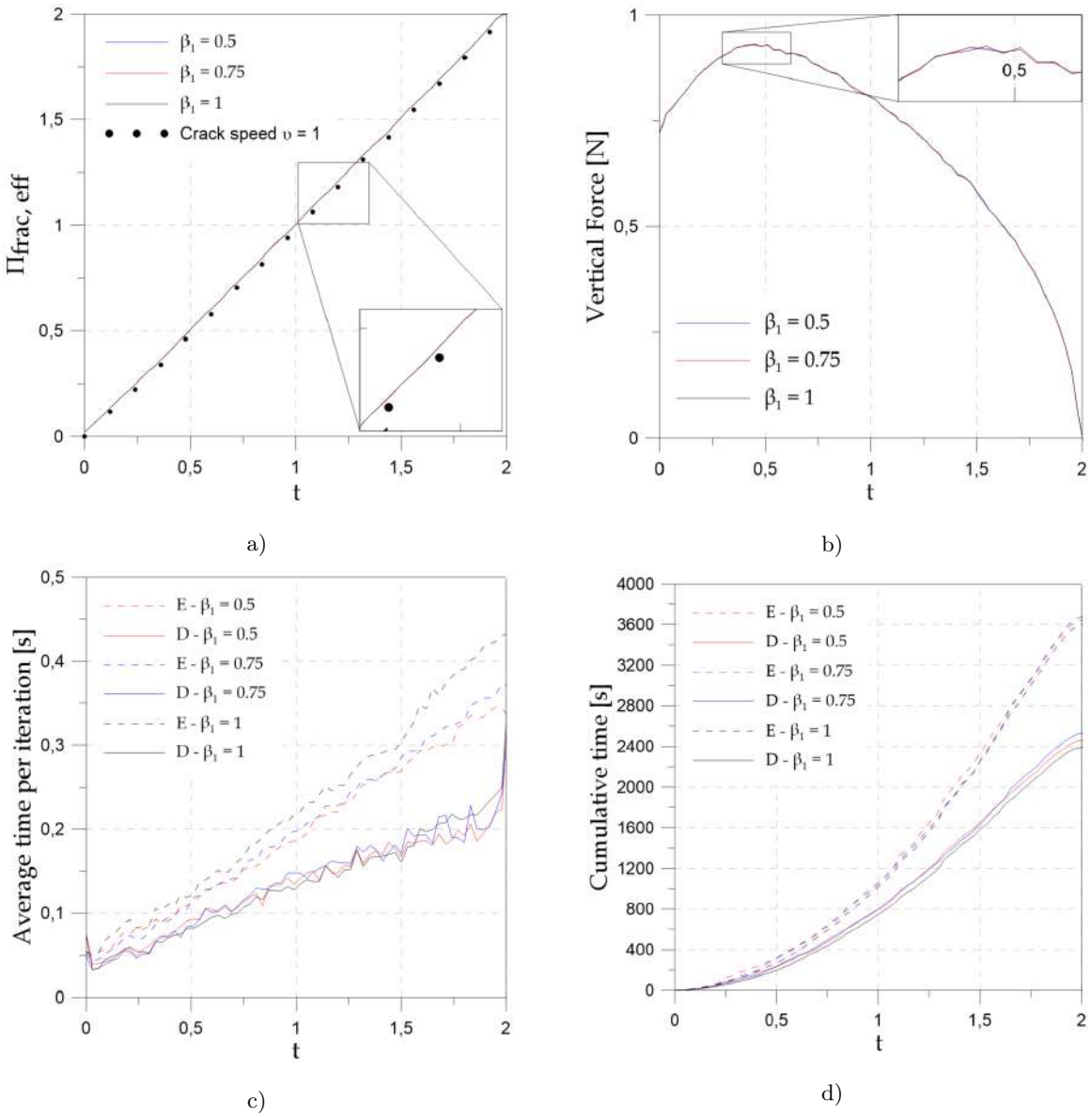

Figure 19: Results of AGu-AGα for different values of β_1: a) Evolution of the effective fracture energy; b) Load-time curves; c) Average time per iteration for the elastic problem (E) and for the damage problem (D); d) Cumulative time for the elastic problem (E) and for the damage problem (D).

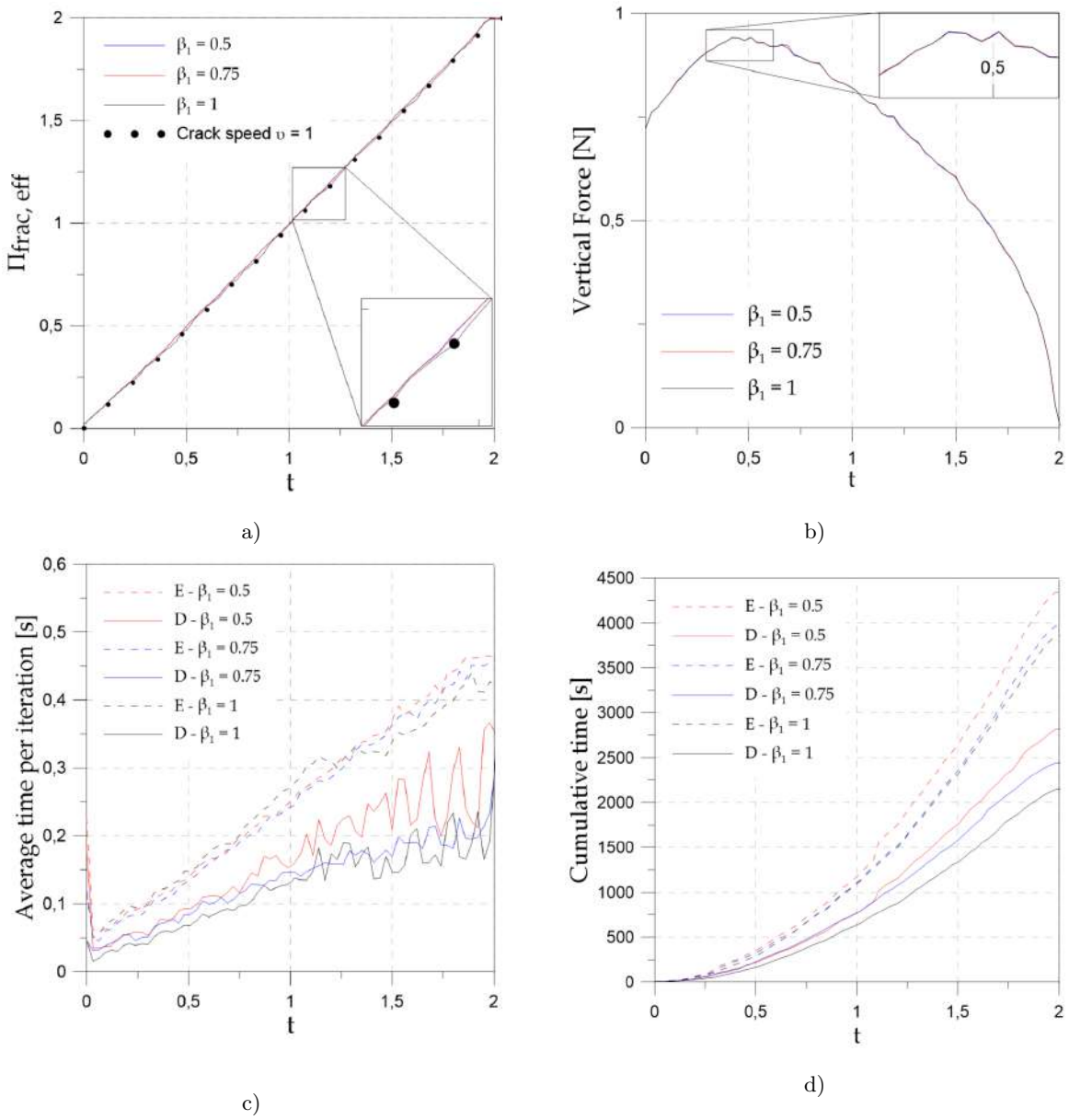

Figure 20: Results of aGu-ALu-ALα for various values of β_1: a) Regularized fracture energy; b) Load-time curves; c) Average time per iteration for the elastic problem (E) and for the damage problem (D); d) Cumulative time for the elastic problem (E) and for the damage problem (D).

- *Inner radius parameter* β_3

The coefficient β_3 which affects the radius of the refined zone around the active elements is varied and set equal to $\beta_3 = \{1, 2, 4\}$. The size of the inner refined area is affected as shown in Fig. 21. In fact, large values of β_3 enlarge the width of the refined zone and lead to high dof number (see Table 7).

Fig. 22 reports the results for the AGu-AGα strategy. Here, the variation of β_3 does not significantly affect the effective fracture energy as shown in Fig. 22a. For the aGu-ALu-ALα strategy it can be seen from Fig. 23a that the insufficient refined area around the fully damaged zone cannot capture correctly the phase field diffusion leading to an overestimation of the fracture energy as the crack length increases. Because of the increased area of the refined zone, the dof changes significantly as outlined in Fig. 23b. A noticeable difference in the computational costs is evidenced in Figs. 23c,d where the average time per

iteration and the cumulative time for the elastic and damage problems are reported.

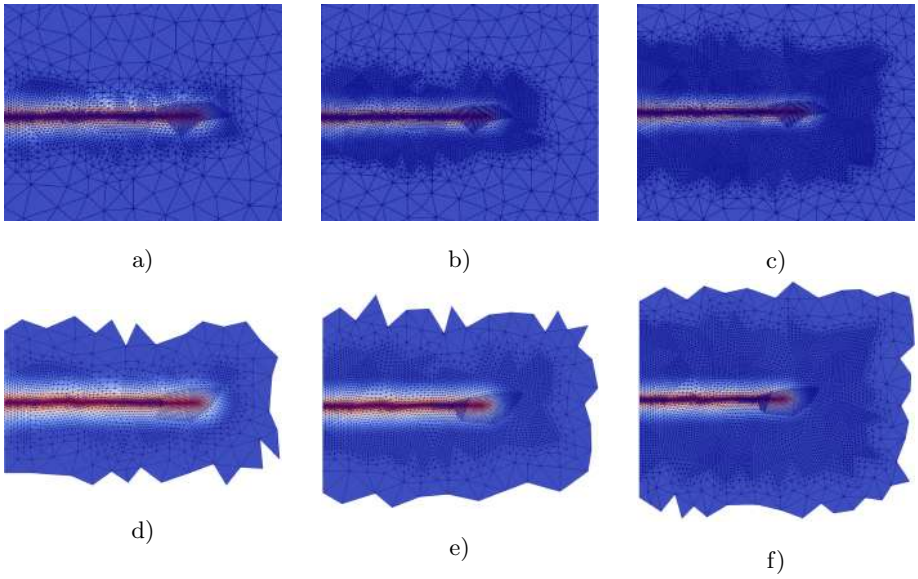

Figure 21: Adaptively refined zone for AGu-AGα and aGu-ALu-ALα for different values of β_3. AGu-AGα: a) 1, b) 2, c) 4. aGu-ALu-ALα: d) 1, e) 2, f) 4

Type	Initial DoF $\mathbf{u}$	Initial DoF α	β_3	Final DoF $\mathbf{u}$	Final DoF α
1 - G$\mathbf{u}$-Gα	225468	112734	-	225468	112734
2 - AG$\mathbf{u}$-AGα	6316	3158	1	35746	17873
			2	49598	24799
			4	75628	37814
3 - aG$\mathbf{u}$-AL$\mathbf{u}$-ALα	4126 (G) - 2280 (L)	1140 (L)	1	21256 (G) - 37486 (L)	18743
			2	21256 (G) - 49890 (L)	24945
			4	21256 (G) - 73022 (L)	36511

Table 7: Degree of freedom of the various optimization procedures at the beginning and at the end of the simulation for different values of β_3 .

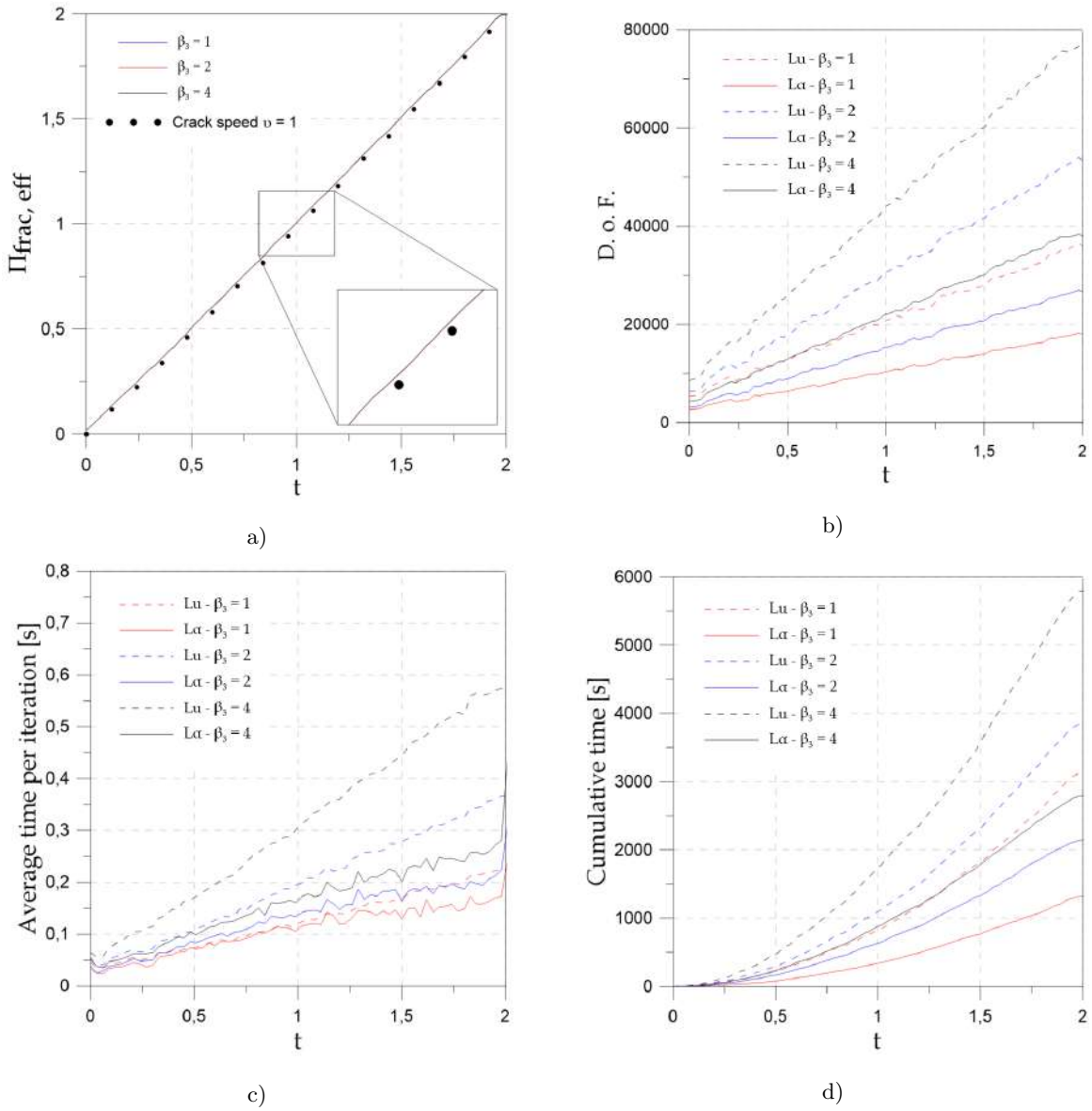

Figure 22: Results of AGu-AGα for various values of β_3 : a) Regularized fracture energy; b) Degrees of freedom for the global elastic(Gu) and damage (Gα) problems; c) Average time per iteration for the elastic problem (E) and for the damage problem (D); d) Cumulative time for the elastic problem (E) and for the damage problem (D).

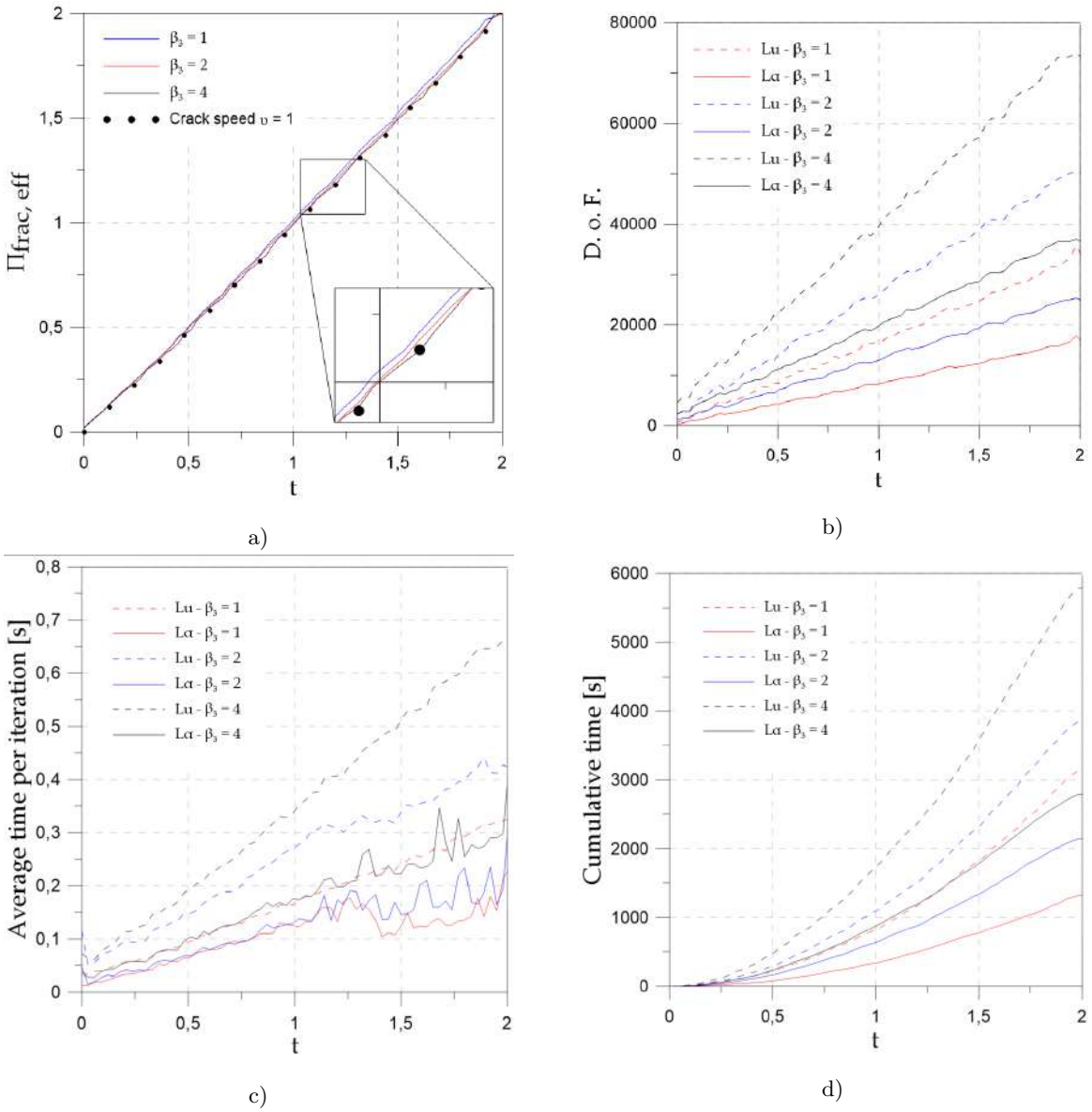

Figure 23: Results of aGu-ALu-ALα for various values of β_3: a) Regularized fracture energy; b) Degrees of freedom for the local elastic (Lu) and damage (Lα) problems; c) Average time per iteration for the elastic problem (E) and for the damage problem (D); d) Cumulative time for the elastic problem (E) and for the damage problem (D).

- *Outer radius parameter* β_2

Now, the parameter β_2, which determines the number of elements around the refined zone, has been set equivalent to $\{1, 2\}$. No significant differences within the results can be noted, both in terms of the fracture energy as well as in the load-time curves as illustrated in Figs. 25a,b. The dof increment is relatively limited as reported in Table 8. A slight increment in the average time per iteration for the elastic problem is observed. Since this parameter affects the number of unrefined outer elements, its value should be consistently taken $\beta_2 \geq 1$, otherwise matching problems between the boundaries of the local and global meshes may occur.

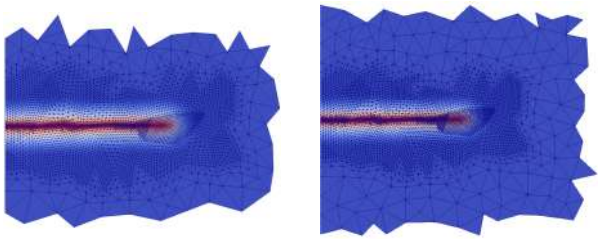

a) b)

Figure 24: Adaptively refined zone for aGu-ALu-ALα for different values of the β_2 parameter: a) 1, b) 2

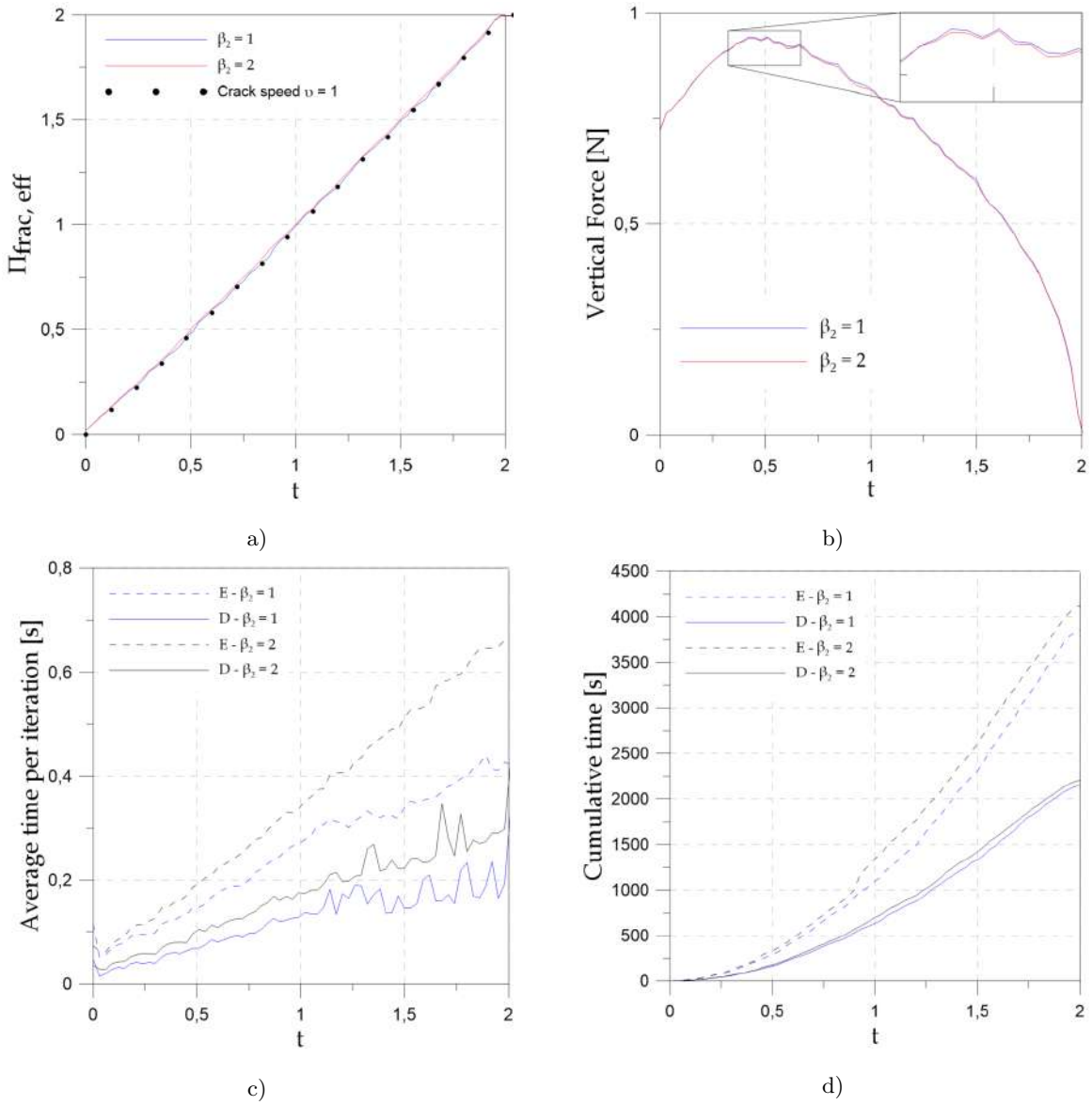

a) b)

c) d)

Figure 25: Results of aGu-ALu-ALα for various values of β_2: a) Regularized fracture energy; b) Load-time curves; c) Average time per iteration for the elastic problem (E) and for the damage problem (D); d) Cumulative time for the elastic problem (E) and for the damage problem (D).

Type	Initial DoF **u**	Initial DoF α	β_2	Final DoF **u**	Final DoF α
aG**u**-AL**u**-ALα	4126 (G) - 2280 (L)	1140 (L)	1	21256 (G) - 49890 (L)	24945
			2	21256 (G) - 50412 (L)	25206

Table 8: Degree of freedom at the beginning and at the end of the simulation for different values of β_2.

- *Damage threshold* α_s

Lastly, the influence of the damage threshold α_s has been investigated. The tests were performed by setting $\alpha_s = \{0.5, 0.9, 0.99\}$. Fig. 26 shows the changes in the global refined mesh for both the refinement strategies. The value of α_s affects the refined area of the active elements where damage is completely developed. The increase of the unknowns reported in Table 9 is evident for the two approaches. Further, the phase field profiles of Figs. 26d,e,f, extrapolated for aGu-ALu-AL, correctly reproduce the fracture topology.

Results for the AGu-AGα strategy are reported in Figs. 27a,b. It can be noted that the global approach is not significantly affected by the choice of the parameter value due to the presence of the surrounding refined elements. However, in Fig. 27c,d the results for the aGu-ALu-ALα strategy highlight that excessive value of α_s can not capture precisely the transition zone between damaged and undamaged areas, leading to oscillations in the load-time plot.

Figs. 27b,d shows the average time per iteration required to solve the elastic and the damage problem. Due to the increment of the dof, the computational time at each iteration increases significantly, almost doubling.

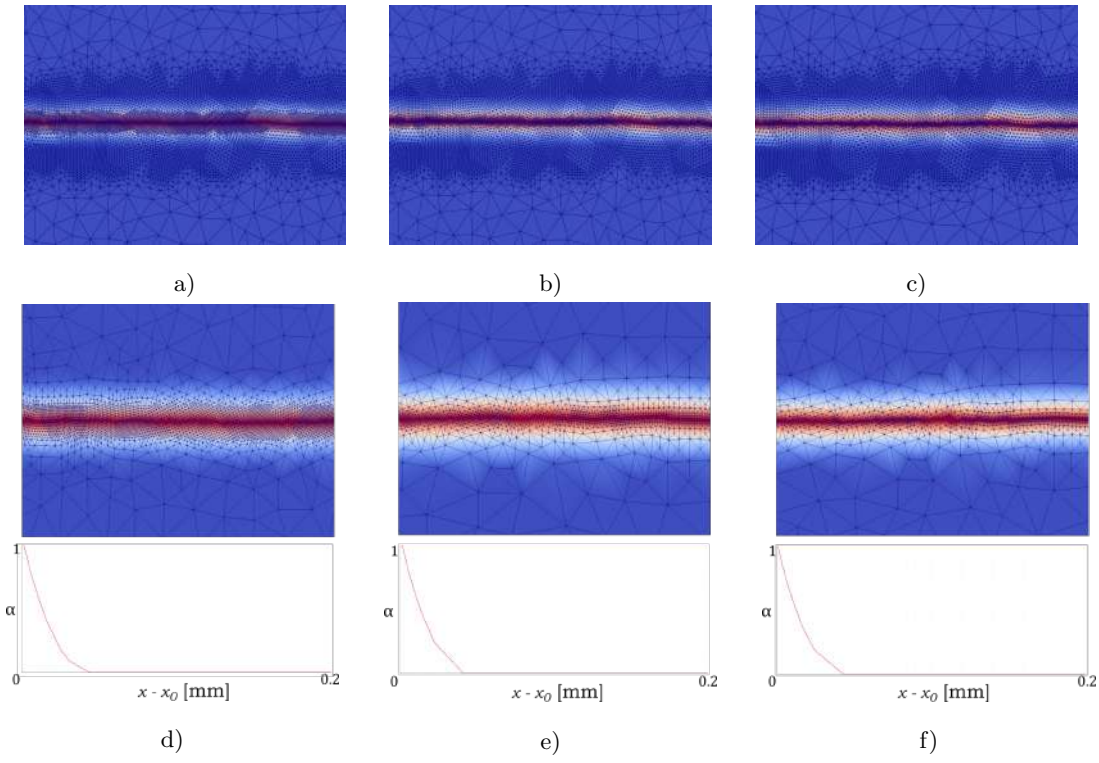

Figure 26: Adaptively refined zone in the global mesh for AGu-AGα and aGu-ALu-ALα for different values of α_s. AGu-AGα: a) $\alpha_s = 0.5$, b) $\alpha_s = 0.9$, c) $\alpha_s = 0.99$. aGu-ALu-AGα: d) $\alpha_s = 0.5$, e) $\alpha_s = 0.9$, f) $\alpha_s = 0.99$. The phase field profile is extrapolated for the three cases.

Type	Initial DoF **u**	Initial DoF α	α_s	Final DoF **u**	Final DoF α
AG**u**-AGα	6316	3158	0.5	67136	33568
			0.9	53018	26509
			0.99	49598	24799
aG**u**-AL**u**-ALα	4126 (G) - 2280 (L)	1140 (L)	0.5	41274 (G) - 63794 (L)	31897
			0.9	21256 (G) - 49890 (L)	24945
			0.99	16416 (G) - 47086 (L)	23543

Table 9: Degree of freedom of the various optimization procedures at the beginning and at the end of the simulation for different values of α_s.

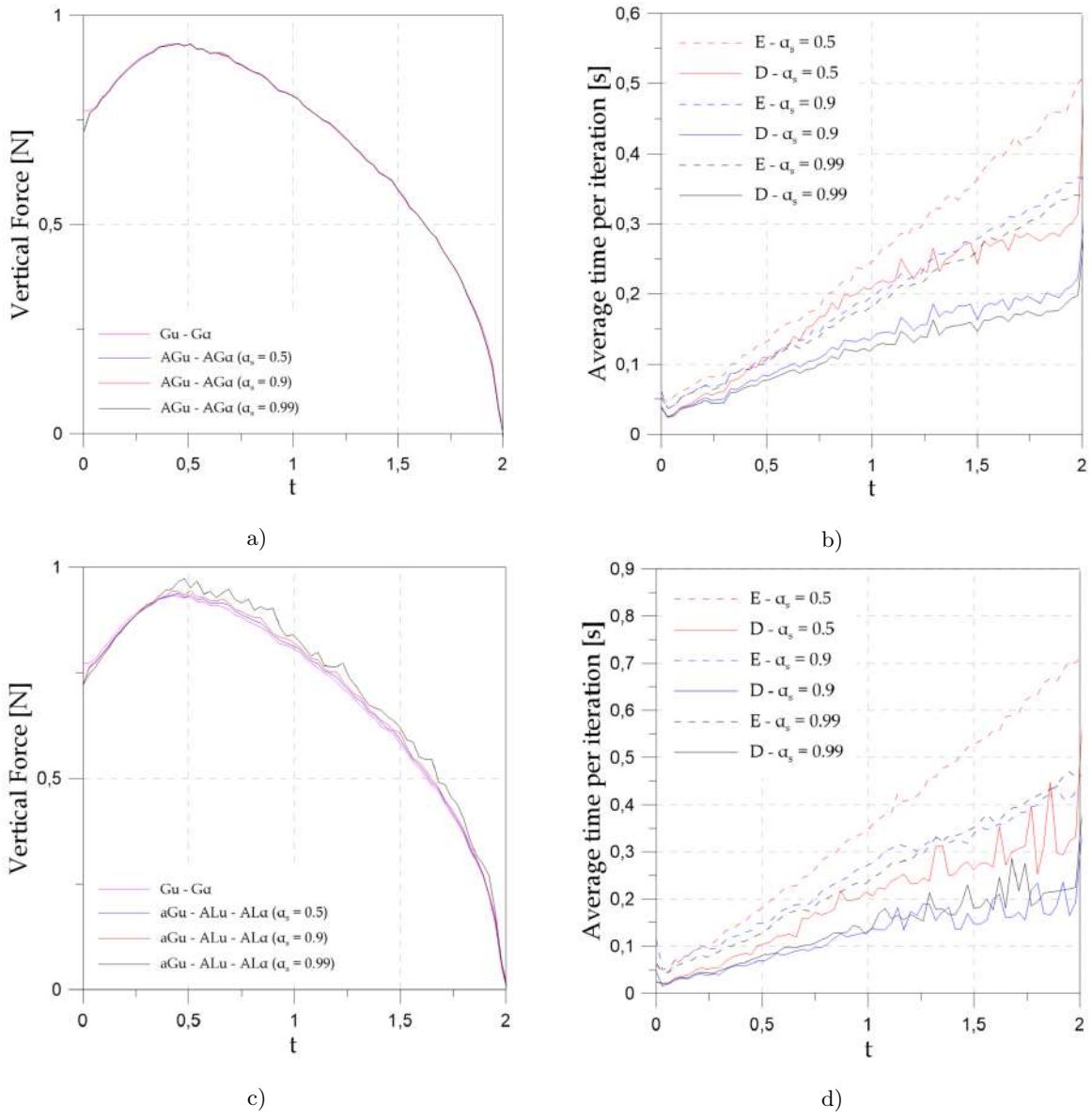

Figure 27: Result comparisons for different α_s values for AGu-AGα and aGu-ALu-ALα. AGu-AGα: a) Load-time curves; b) Average time per iteration at each time step. The dashed lines refer to the elastic problem (E), the continuous lines refer to the damage problem (D). aGu-ALu-ALα: c) Load-time curves; d) Average time per iteration at each time step. The dashed lines refer to the elastic problem (E), the continuous lines refer to the damage problem (D).

6.3. Abrupt crack propagation test

A case where the crack pattern is a priori unknown is studied. As shown in Section 5, a square plate with three pre-existing cracks is taken into account. Figs. 28, 29, 30 report the damage maps at two load steps for Gu-Gα, AGu-AGα and aGu-ALu-ALα respectively. Two abrupt fracture propagations occur. The simulation stops once the solid has broken into four independent pieces. The crack patterns obtained with the two refinement strategies at the first fracture growth as well as at the end of the simulation coincide with the one achieved with the reference test.

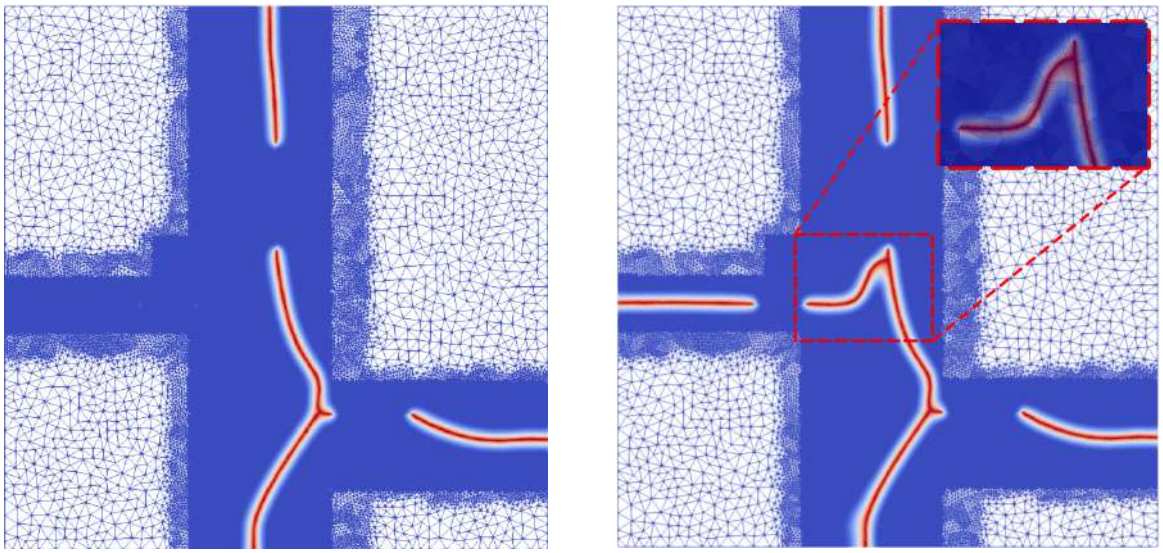

a) b)

Figure 28: Phase field maps at two load steps for Gu-Gα: a) Global refined mesh at $\bar{u} = 0.0015\,mm$; b) Global refined mesh at $\bar{u} = 0.003\,mm$.

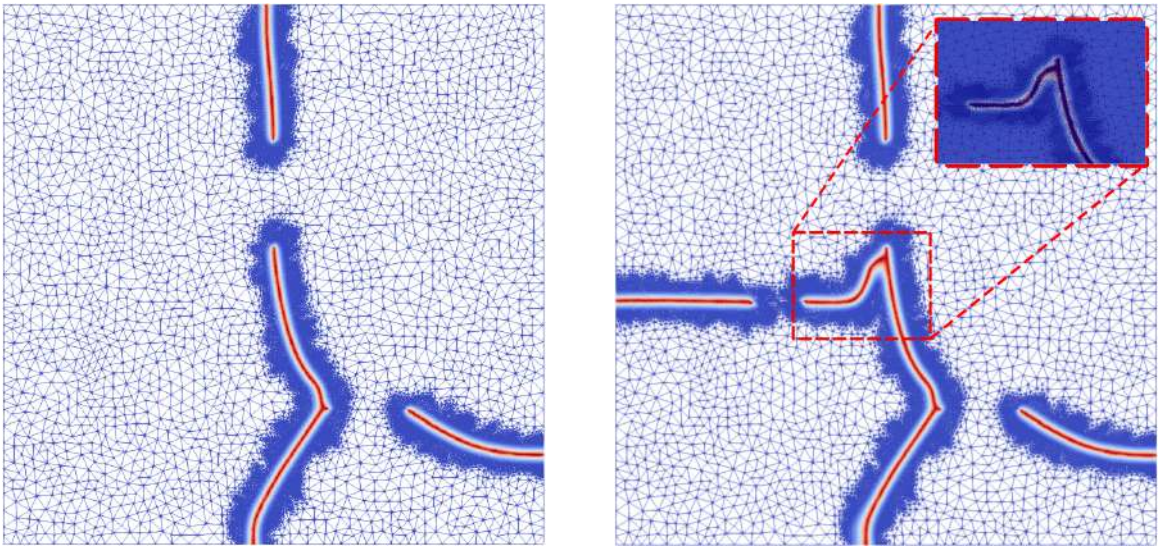

a) b)

Figure 29: Phase field maps at two load steps for AGu-AGα: a) Global refined mesh at $\bar{u} = 0.0015\,mm$; b) Global refined mesh at $\bar{u} = 0.003\,mm$.

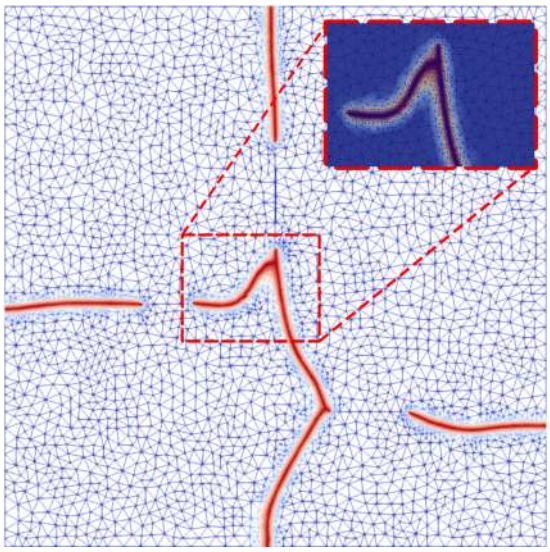

a)

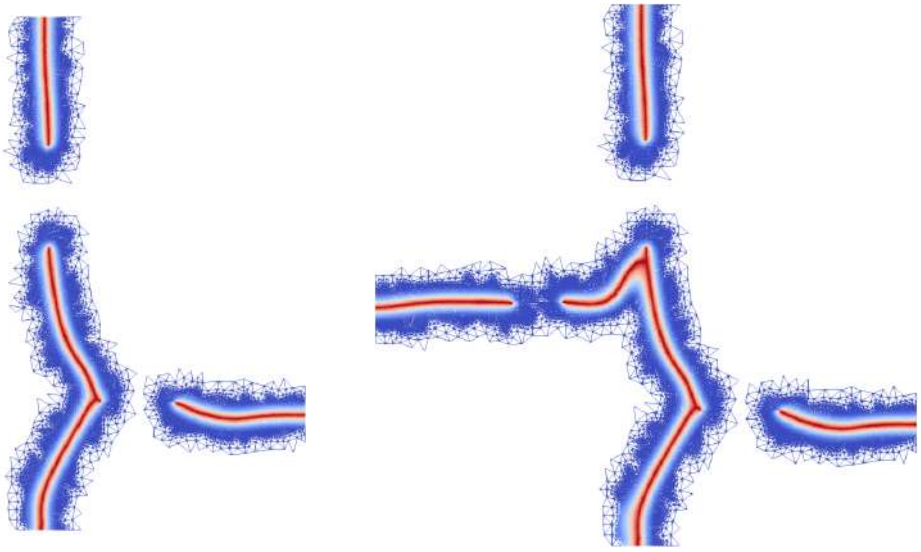

b) c)

Figure 30: Phase field maps for aGu-ALu-ALα: a) Global refined mesh at $\bar{u} = 0.003\,mm$; b) Local mesh at $\bar{u} = 0.0015\,mm$; c) Local mesh at $\bar{u} = 0.003\,mm$.

The load-displacement diagrams for both the horizontal and the vertical loads are plotted in Fig. 31. The abrupt propagation coincides with a drop in the curves. The horizontal stiffness is lost as a fracture divides vertically the solid at $\bar{u} = 0.0015\,mm$. Subsequently, the plate is cut horizontally by a crack crossing the entire width. The load paths are almost identical for the refinement strategies. Figs. 32a,b report the evolution of the elastic, fracture energies as a function of the imposed displacement. The different refinement strategies are compared. As seen in the previous test, the different types of refinement show good agreement with the reference solution. The same drops of the load-displacement curves are evidenced in the elastic energy evolution whereas rapid increments of the fracture energy are the consequence of the brutal crack propagations.

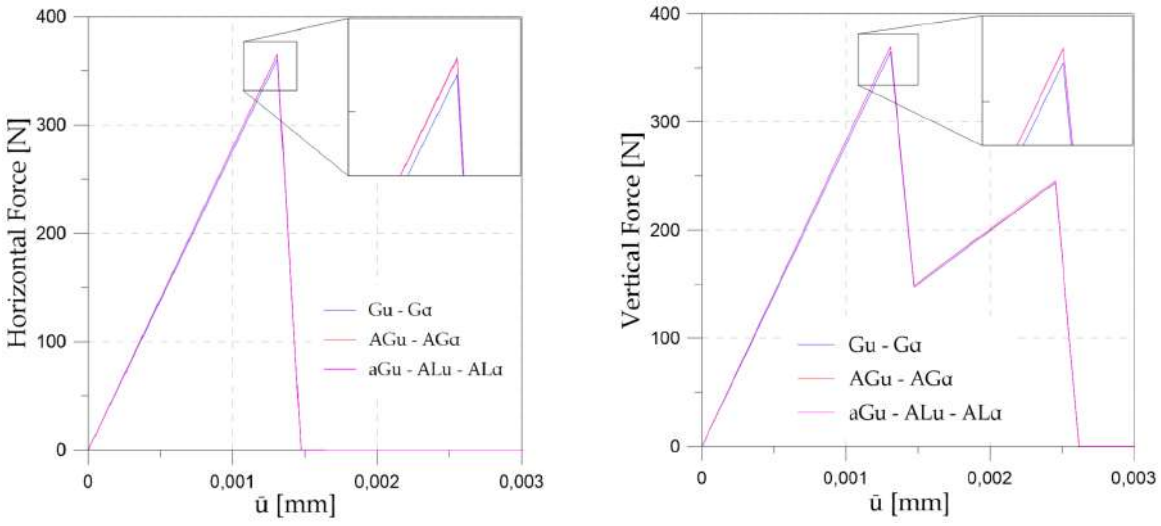

e) f)

Figure 31: Load-displacement curves for the abrupt crack test: a) horizontal force; b) vertical force.

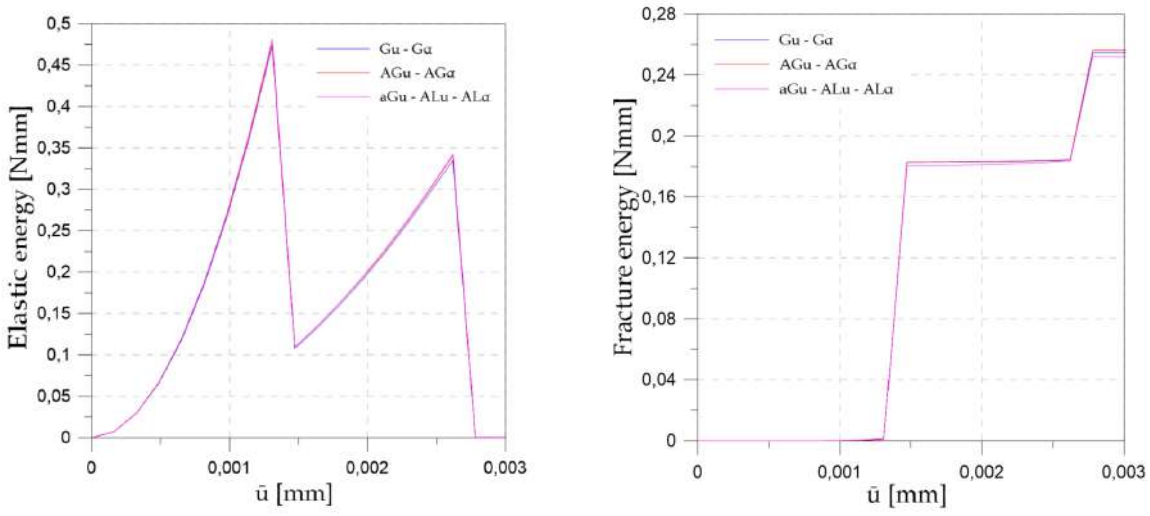

c) d)

Figure 32: Energy evolutions for the abrupt crack test: a) elastic energy; d) fracture energy .

Fig. 33 summarizes the computational costs for the different solution strategies. In Fig. 33a,b the dof for the elastic and damage problems are reported as a function of the imposed displacement. The reference test presents a number of dof at least one order of magnitude greater than the ones of the refinement procedures. Accordingly, the computational times, reported in Fig. 33c,d for the elastic and damage problems as a function of the imposed displacement, are significantly quicker for refinement strategies. The spike in the time required for the solution of the elastic and damage problems corresponds to brutal crack advancement. Finally, in Table 10 the total computational times for the different refinement strategy are listed. The reduction in the required time to perform the complete simulation for the different optimization procedures compared against the benchmark test is significant. The computational savings of adaptivity techniques are quite similar. The global/local strategy, as in the previous example, performs better in

terms of computation time because fewer iterations are required in the alternate minimization algorithm. For completeness, the values of the initial and final degrees of freedom for each optimization procedure are also reported in Table 11.

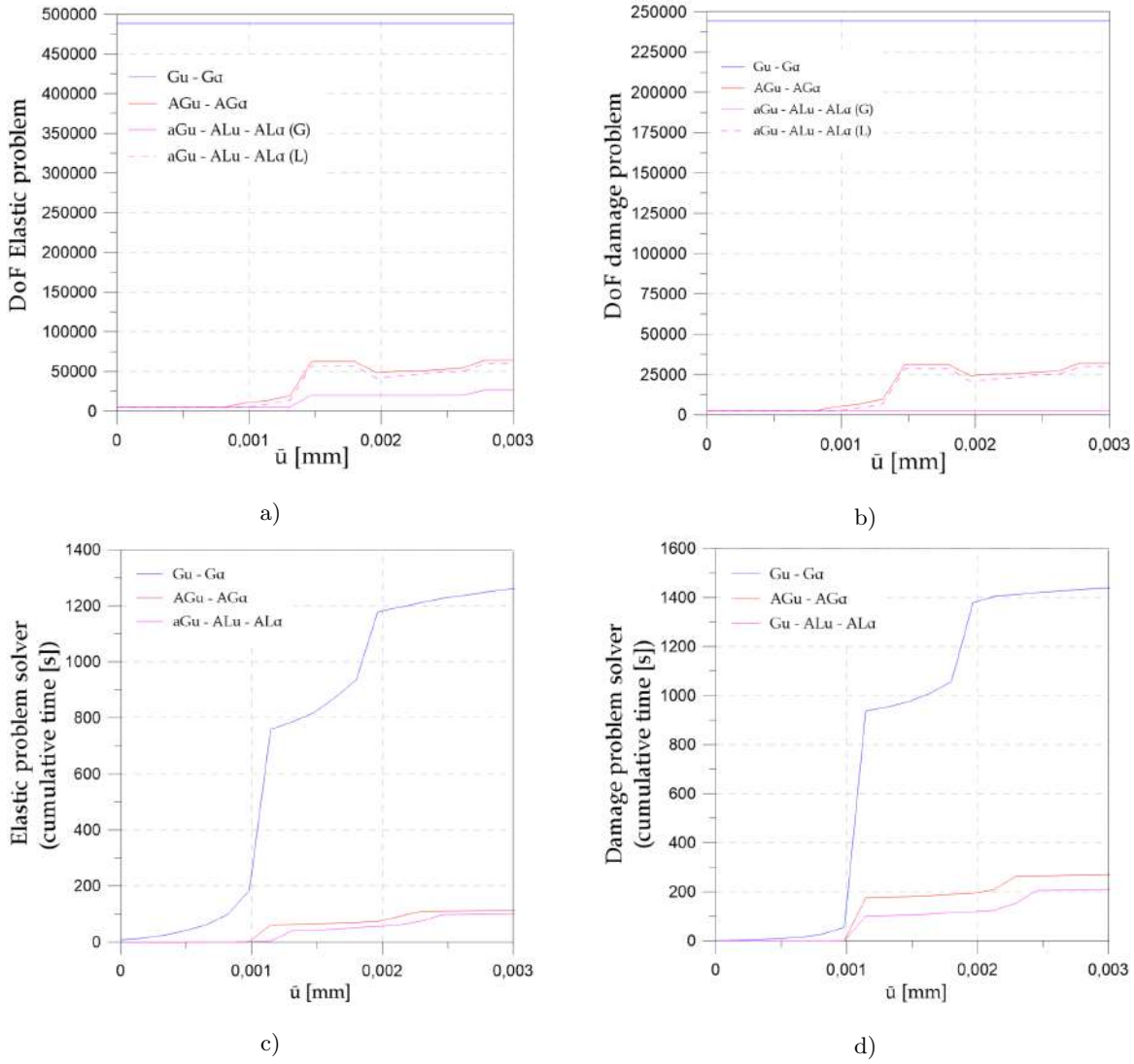

Figure 33: Computational costs for the abrupt damage test: a) Degrees of freedom of the elastic problem; b) Degrees of freedom the damage problem; c) Cumulative time for the elastic problem; d) Cumulative time for the damage problem.

Type	Total computational time [s]	Time reduction (%)
1 - G**u**-Gα	2724	-
2 - AG**u**-AGα	387	85%
3 - aG**u**-AL**u**-ALα	315	89%

Table 10: Abrupt crack propagation test: total computational time and the corresponding percentage reduction in the required time to run the complete simulation for the different optimization procedures compared against the reference test.

Type	Initial DoF **u**	Initial DoF α	Final DoF **u**	Final DoF α
1 - G**u**-Gα	488376	244188	488376	244188
2 - AG**u**-AGα	5112	2556	58714	29357
3 - aG**u**-AL**u**-ALα	5112 (G) - 4830 (L)	2415 (L)	26414 (G) - 54762 (L)	27381 (L)

Table 11: Degree of freedom of the various optimization procedures at the beginning and at the end of the simulation.

7. Conclusion

Two refinement procedures for phase field approach have been proposed and their numerical performances have been compared. The strategies have demonstrated a remarkable performance increment in term of computational costs with respect to the classic approach with fully refined mesh. The adopted criterion permits the correct individuation of the active zones characterized by crack nucleation and advancement, allowing the study of the phase field evolution on a adaptively refined mesh defined from an initial coarse one. The refinement performed in the active regions does not alter the process of fracture initiation, propagation and bifurcation as demonstrated by the proposed examples.

The most convenient approach in term computational costs is the local/global one that offers a reduction in calculation time of about $20 - 30\%$ with respect to a global refinement technique although it has demonstrated higher sensitivity to the choice of parameters. In fact, the solution and the computational costs obtained with the aGu-ALu-ALα strategy showed a certain dependency on the choice of the damage threshold α_s and the inner radius coefficient β_3. The damage threshold α_s highly affects the accuracy of the results, as the refined zone on the global mesh may fail to reproduce correctly the kinematics of a fracture. The parameter β_3 has an important impact on the refinement strategy efficiency and accuracy since it defines the size of the refined area. In fact, refined area smaller than the width of the optimal damage profile lead to an unrefined portion of the mesh in the transition zone, whereas too large refinement zone has the consequence to increase the computational costs without precision increase.

The following suggestions, based upon the computational experience, are given for the choice of the parameter values:

α_s**:** values $\in [0.8, 0.9]$ offer good precisions and keep computational cost limited;

β_1**:** values $\in [0.75, 1]$ permit to correctly catch the active zones without influencing significantly the computational costs;

β_2**:** values $\in [1, 1.25]$ values determine perfect matching between the boundaries of the local and global meshes;

β_3**:** value 2 permits to correctly catches the entire transition zone according to the optimal damage profile extension; in case the optimal profile is not guaranteed different values should be considered.

The proposed adaptive strategies can be easily implemented into existing FEM code to speed up computational times in any formulation based on energetic damage criterion [62]. Moreover, with minimal modification the proposed procedures can be implemented in the case of exponential optimal phase field profile. In addition, the global approach could be coupled with monolithic quasi-Newton solving techniques to speed up computations. In a forthcoming work the global/local technique will be adopted to ensure continuity of the unknowns in a variational way to avoid the transition zone between the two meshes. A further performance increment of the approach can be obtained by adopting Lagrange multiplier techniques for the imposition of boundary conditions on the local mesh or treating hanging nodes effectively. Lastly, mesh de-refinement could further improve the procedure performances, however it is a very delicate issue. On the one hand, a certain amount of refinement must be guaranteed in order to capture the mechanical discontinuity and any new nucleation in areas previously affected by fracture phenomena, on the other hand it would be extremely effective to restrict the solution of the damage problem to the area in which an evolution of the phase field occurs.

References

[1] A. A. Griffith, The phenomena of rupture and flow in solids, Philosophical Transactions of the Royal Society of London A221 (1921) 163–198.

[2] G. A. Francfort, J.-J. Marigo, Revisiting brittle fracture as an energy minimization problem, J. Mech. Phys. Solids 46 (1998) 1319–1342.

[3] B. Bourdin, G. A. Francfort, J.-J. Marigo, Numerical experiments in revisited brittle fracture, J. Mech. Phys. Solids 48 (2000) 797–826.

[4] H. Amor, J.-J. Marigo, C. Maurini, Regularized formulation of the variational brittle fracture with unilateral contact: Numerical experiments, Journal of the Mechanics and Physics of Solids 57 (2009) 1209 – 1229.

[5] F. Freddi, G. Royer-Carfagni, Regularized variational theories of fracture: A unified approach, Journal of the Mechanics and Physics of Solids 58 (2010) 1154 – 1174.

[6] F. Freddi, G. Royer-Carfagni, Variational fracture mechanics to model compressive splitting of masonry-like materials, Annals of Solid and Structural Mechanics 2 (2011) 57–67.

[7] A. Chambolle, S. Conti, G. A. Francfort, Approximation of a brittle fracture energy with a constraint of non-interpenetration, Arch. Rational Mech. Anal. 228 (2018) 867–889.

[8] G. Lancioni, G. Royer-Carfagni, The variational approach to fracture mechanics. a practical application to the french panthéon in paris, Journal of Elasticity 95 (2009) 1–30.

[9] R. Alessi, F. Freddi, L. Mingazzi, Phase-field numerical strategies for deviatoric driven fractures, Comput. Methods in Appl. Mech. Eng. 359 (2020).

[10] R. Alessi, J.-J. Marigo, S. Vidoli, Gradient Damage Models Coupled with Plasticity and Nucleation of Cohesive Cracks, Archive for Rational Mechanics and Analysis 214 (2014) 575–615.

[11] R. Alessi, J.-J. Marigo, S. Vidoli, Gradient damage models coupled with plasticity: Variational formulation and main properties, Mechanics of Materials 80 (2015) 351–367.

[12] M. Ambati, T. Gerasimov, L. De Lorenzis, Phase-field modeling of ductile fracture, Comput. Mech. 55 (2015) 1017–1040.

[13] R. Alessi, J.-J. Marigo, C. Maurini, S. Vidoli, Coupling damage and plasticity for a phase-field regularisation of brittle, cohesive and ductile fracture: One-dimensional examples, International Journal of Mechanical Sciences 149 (2018) 559–576.

[14] F. Freddi, G. Royer-Carfagni, Plastic flow as an energy minimization problem. Numerical experiments, Journal of Elasticity 116 (2014) 53–74.

[15] F. Freddi, G. Royer-Carfagni, Phase-field slip-line theory of plasticity, Journal of the Mechanics and Physics of Solids 94 (2016) 257–272.

[16] P. K. Kristensen, C. F. Niordson, E. Martínez-Pañeda, A phase field model for elastic-gradient-plastic solids undergoing hydrogen embrittlement, J. Mech. Phys 143 (2020).

[17] R. Alessi, F. Freddi, Failure and complex crack patterns in hybrid laminates: A phase-field approach, Composites Part B: Engineering 179 (2019) 107256.

[18] A. A. León Baldelli, J. F. Babadjian, B. Bourdin, D. Henao, C. Maurini, A variational model for fracture and debonding of thin films under in-plane loadings, Journal of the Mechanics and Physics of Solids 70 (2014) 320–348.

[19] R. Alessi, F. Freddi, Phase-field modelling of failure in hybrid laminates, Composite Structures 181 (2017) 9 – 25.

[20] F. Freddi, L. Mingazzi, Phase field simulation of laminated glass beam, Materials 13 (2020).

[21] F. Freddi, F. Iurlano, Numerical insight of a variational smeared approach to cohesive fracture, Journal of the Mechanics and Physics of Solids 98 (2017) 156 – 171.

[22] J.-Y. Wu, A unified phase-field theory for the mechanics of damage and quasi-brittle failure, Journal of the Mechanics and Physics of Solids 103 (2017) 72 – 99.

[23] S. M. Dsouza, H. Hirshikesh, T. V. Mathew, I. V. Singh, S. Natarajan, A non-intrusive stochastic phase field method for crack propagation in functionally graded materials, Acta Mech 232 (2021) 2555–2574.

[24] P. Carrara, M. Ambati, R. Alessi, L. De Lorenzis, A framework to model the fatigue behavior of brittle materials based on a variational phase-field approach, Computer Methods in Applied Mechanics and Engineering 361 (2020) 112731.

[25] L. Ambrosio, V. M. Tortorelli, Approximation of functionals depending on jumps by elliptic functionals via Γ-convergence, Comm. Pure Appl. Math. 43 (1990) 999–1036.

[26] T. Heister, M. F. Wheeler, T. Wick, A primal-dual active set method and predictor-corrector mesh adaptivity for computing fracture propagation using a phase-field approach, Comput. Methods Appl. Mech. Engrg 290 (2015) 466–495.

[27] H.-Y. Kim, H.-G. Kim, A novel adaptive mesh refinement scheme for the simulation of phase-field fracture using trimmed hexahedral meshes, International Journal for Numerical Methods in Engineering 122 (2021) 1493–1512.

[28] H. Hirshikesh, E. Martínez-Pañeda, S. Natarajan, Adaptive phase field modelling of crack propagation in orthotropic functionally graded materials, Defence Technology 17 (2021) 185–195.

[29] A. Muixì, S. Fernàndez-Mèndez, A. Rodrìguez-Ferran, Adaptive refinement for phase-field models of brittle fracture based on nitsche's method, Computational Mechanics 66 (2020) 69–85.

[30] F. Tian, X. Tang, T. Xu, J. Yang, L. Li, A hybrid adaptive finite element phase-field method for quasi-static and dynamic brittle fracture, International Journal for Numerical Methods in Engineering 120 (2019) 1108–1125.

[31] S. Zhou, X. Zhuang, Adaptive phase field simulation of quasi-static crack propagation in rocks, Underground Space 3 (2018) 190–205.

[32] H. Hirshikesh, A. L. N. Pramod, R. K. Annabattula, E. T. Ooi, C. Song, S. Natarajan, Adaptive phase-field modeling of brittle fracture using the scaled boundary finite element method, Comput. Methods Appl. Mech. Engrg 355 (2019) 284–307.

[33] H. Hirshikesh, A. L. N. Pramod, H. Waisman, S. Natarajan, Adaptive phase field method using novel physics based refinement criteria, Computer Methods in Applied Mechanics and Engineering 383 (2021).

[34] P. Areias, M. A. Msekh, T. Rabczuk, Damage and fracture algorithm using the screened poisson equation and local remeshing, Engineering Fracture Mechanics 158 (2016).

[35] P. Areias, J. Reinoso, P. P. Camanho, J. César de Sá, T. Rabczuk, Effective 2D and 3D crack propagation with local mesh refinement and the screened poisson equation, Engineering Fracture Mechanics 189 (2018).

[36] T. Gerasimov, N. Noii, O. Allix, L. De Lorenzis, A non-intrsive global/local approach applied to phase-field modeling of brittle fracture, Adv. Model. and Simul. in Eng. Sci. 5 (2018).

[37] F. Aldakheel, N. Noii, T. Wick, P. Wriggers, A global–local approach for hydraulic phase-field fracture in poroelastic media, Computers & Mathematics with Applications 91 (2021) 99–121. Robust and Reliable Finite Element Methods in Poromechanics.

[38] F. Aldakheel, N. Noii, T. Wick, O. Allix, P. Wriggers, Multilevel global-local techniques for adaptive ductile phase-field fracture, 2021. arXiv:2103.02377.

[39] N. Noii, F. Aldakheel, T. Wick, P. Wriggers, An adaptive global–local approach for phase-field modeling of anisotropic brittle fracture, Computer Methods in Applied Mechanics and Engineering 361 (2020) 112744.

[40] R. Geelen, J. Plews, M. Tupek, J. Dolbow, An extended/generalized phase-field finite element method for crack growth with global-local enrichment, International Journal for Numerical Methods in Engineering 121 (2020) 2534–2557.

[41] R. Patil, B. Mishra, I. Singh, An adaptive multiscale phase field method for brittle fracture, Comput. Methods Appl. Mech. Engrg 329 (2018) 254–288.

[42] R. U. Patil, B. K. Mishra, I. V. Singh, A local moving extended phase field method (lmxpfm) for failure analysis of brittle materials, Comput. Methods Appl. Mech. Engrg. 342 (2018) 674–709.

[43] E. Samaniego, C. Anitescu, S. Goswami, V. M. Nguyen-Thanh, H. Guo, K. Hamdia, X. Zhuang, T. Rabczuk, An energy approach to the solution of partial differential equations incomputational mechanics via machine learning: Concepts,implementation and applications, Computer Methods in Applied Mechanics and Engineering 362 (2020).

[44] A. Pandolfi, K. Weinberg, M. Ortiz, A comparative accuracy and convergence study of eigenerosion and phase- field models of fracture, 2021. arXiv:2101.12520.

[45] G. Bellettini, A. Coscia, Discrete approximation of a free discontinuity problem, Numer. Funct. Anal. Optim. 15 (1994) 201–224.

[46] B. Bourdin, G. A. Francfort, J.-J. Marigo, The variational approach to fracture, J. Elasticity 91 (2008) 5–148.

[47] K. Pham, H. Amor, J.-J. Marigo, C. Maurini, Gradient damage models and their use to approximate brittle fracture, International Journal of Damage Mechanics 20 (2011) 618–652.

[48] M. J. Borden, T. J. Hughes, C. M. Landis, C. V. Verhoosel, A higher-order phase-field model for brittle fracture: Formulation and analysis within the isogeometric analysis framework, Computer Methods in Applied Mechanics and Engineering 273 (2014) 100 – 118.

[49] L. De Lorenzis, T. Gerasimov, Numerical Implementation of Phase-Field Models of Brittle Fracture, Springer International Publishing, Cham, 2020, pp. 75–101.

[50] B. Bourdin, Numerical implementation of the variational formulation for quasi-static brittle fracture, Interfaces Free Bound. 9 (2007) 411–430.

[51] S. Burke, C. Ortner, E. Süli, An adaptive finite element approximation of a generalized ambrosio-tortorelli functional, Mathematical Models and Methods in Applied Sciences 23 (2013) 1663–1697.

[52] W. Bangerth, R. Hartmann, G. Kanschat, deal.II – a general purpose object oriented finite element library, ACM Trans. Math. Softw. 33 (2007) 24/1–24/27.

[53] L. Anders, M. Kent-Andre, G. Wells, Automated Solution of Differential Equations by th Finite Elmenet Method - The FEniCS Book, volume 84 of *Lecture notes in computational science and engineering*, Springer, 2012.

[54] S. Balay, S. Abhyankar, M. F. Adams, J. Brown, P. Brune, K. Buschelman, L. Dalcin, A. Dener, V. Eijkhout, W. D. Gropp, D. Kaushik, M. G. Knepley, D. A. May, L. C. McInnes, R. T. Mills, T. Munson, K. Rupp, P. Sanan, B. F. Smith, S. Zampini, H. Zhang, H. Zhang, PETSc Web page, 2018. URL: http://www.mcs.anl.gov/petsc.

[55] F. Freddi, L. Mingazzi, A fenics implementation of the phase field method for quasi-static brittle fracture with adaptive refinement, 2021. In preparation.

[56] The SciPy community, scipy.spatial.ckdtree, 2021. URL: https://docs.scipy.org/doc/scipy/reference/generated/%scipy.spatial.cKDTree.html.

[57] M. Hossain, C.-J. Hsueh, B. Bourdin, K. Bhattacharya, Effective toughness of heterogeneous media, J. Mech. Phys. Solids 71 (2014) 15–32.

[58] J.-J. Marigo, C. Maurini, K. Pham, An overview of the modelling of fracture by gradient damage models, Meccanica 51 (2016) 3107–3128.

[59] P. Farrell, C. Maurini, Linear and nonlinear solvers for variational phase-field models of brittle fracture, International Journal for Numerical Methods in Engineering 109 (2017) 648–667.

[60] F. Aldakheel, N. Noii, T. Wick, P. Wriggers, An existence result for a model of complete damage in elastic materials with reversible evolution, Continuum Mech. Thermodyn. 29 (2017) 31–50.

[61] F. Freddi, Fracture energy in phase field models, Mechanics Research Communications 96 (2019) 29 – 36.

[62] L. De Lorenzis, C. Maurini, Nucleation under multi-axial loading in variational phase-field models of brittle fracture, International Journal of Fracture (2021).